International Journal of Heat and Mass Transfer 240 (2025) 126593

Contents lists available at ScienceDirect

International Journal of Heat and Mass Transfer

journal homepage: www.elsevier.com/locate/ijhmt

Pressure drop characteristics and prediction techniques (models/correlations and artificial neural networks) for microgravity flow boiling onboard the International Space Station

Issam Mudawar [a,*], Steven J. Darges [a], V.S. Devahdhanush [a], Mohammad M. Hasan [b], Henry K. Nahra [b], R. Balasubramaniam [c], Jeffrey R. Mackey [d]

[a] Purdue University Boiling and Two-Phase Flow Laboratory (PU-BTPFL), School of Mechanical Engineering, Purdue University, 585 Purdue Mall, West Lafayette, IN 47907, USA
[b] NASA Glenn Research Center, 21000 Brookpark Road, Cleveland, OH 44135, USA
[c] Case Western Reserve University, 10900 Euclid Ave., Cleveland, OH 44106, USA
[d] HX5, LLC 3000 Aerospace Parkway, Brookpark, OH 44142, USA

ARTICLE INFO

Keywords:
flow boiling
microgravity
pressure drop
prediction techniques
machine learning
correlation assessment
International Space Station

ABSTRACT

This article is part of the multi-objective Flow Boiling and Condensation Experiment (FBCE) onboard the International Space Station, which utilized the Flow Boiling Module (FBM) for experiments during February – July 2022. This study investigates pressure drop characteristics of microgravity flow boiling of n-Perfluorohexane in FBM's rectangular channel of 5.0 × 2.5 mm^2 cross-sectional area and 114.6 mm heated length. Both subcooled and saturated inlet conditions are studied, while one or two opposite walls of the four are uniformly heated, to amass a large database of 3393 datapoints. Operating parameters explored include mass velocity (180.0 – 3200.1 kg/m^2s), inlet quality (-0.62 – 0.87, corresponding to inlet subcooling of 46.0 – 0°C), inlet pressure (119.6 – 200.4 kPa), wall heat flux (< 55.1 W/cm^2), and heating configuration (one or two opposite walls heated). Pressure drop typically increases with increasing mass velocity, increasing inlet quality (for fixed mass velocity), and increasing heat flux (until a point after which it asymptotically reaches a plateau), and is higher for double-sided heating. Inlet pressure did not have an appreciable effect. The primary reason for most of these physical trends is flow acceleration increasing bulk flow velocities and both frictional and accelerational components of pressure drop. Only 2478 datapoints (with smaller experimental uncertainties) are considered for further analysis and assessment of prediction tools. 1099 purely saturated flow boiling datapoints are used to assess 7 mixture viscosity models used with the Homogeneous Equilibrium Model (HEM) and 17 empirical correlations used with the Separated Flow Model (SFM). Of these, the original SFM proposed by Lockhart and Martinelli (1949) is most accurate with a 17.1% mean absolute error (MAE). 1065 purely subcooled flow boiling datapoints are used to assess 9 seminal correlations, of which, the one by Hahne *et al.* (1993) is most accurate with 34.1% MAE. Finally, following a statistical analysis of input parameters, an artificial neural network with 6 hidden layers is developed and trained using the Adam algorithm. It accurately predicts the testing subset of the entire database with a 5.24% MAE, while conforming to expected physical trends in previously unseen data.

1. Introduction

1.1. Flow Boiling for Future Space Missions

Future space missions involve several heat producing systems such as electronics, energy conversion equipment, Fission Power Systems based on the Rankine cycle, and onboard life support systems. Thermal management of these high-power-density systems, and thereby high-heat-flux surfaces, is possible by two-phase schemes [1]. This has been a research focus of the Purdue University Boiling and Two-Phase Flow Laboratory (PU-BTPFL), where both fundamental and applied research since the 1980s on capillary flows [2], pool boiling [3], falling films [4], flow boiling in channels [5], impinging jets [6], sprays [7], and hybrid

* Author to whom correspondence should be addressed: Tel. (765) 494-5705; Fax (765) 494-0539; Website:
E-mail address: mudawar@ecn.purdue.edu (I. Mudawar).
URL: https://engineering.purdue.edu/BTPFL (I. Mudawar).

https://doi.org/10.1016/j.ijheatmasstransfer.2024.126593
Received 15 August 2024; Received in revised form 30 October 2024; Accepted 15 December 2024
Available online 30 December 2024
0017-9310/© 2024 Elsevier Ltd. All rights are reserved, including those for text and data mining, AI training, and similar technologies.

Nomenclature

A_c	cross-sectional area of channel [m^2]
Bd	Bond number, $g(\rho_f - \rho_g)D_h^2/\sigma$
Be	Bejan number, $\Delta pL^2/\mu_f\nu_f$
Bo	boiling number, q''_w/Gh_{fg}
b	bias in ANN
C	empirical constant
c_p	specific heat at constant pressure [J/kg.K]
D	diameter [m]
D_e	equivalent heated diameter, $4A_c/P_h$, [m]
D_h	hydraulic diameter [m]
E	loss in ANN
f	Fanning friction factor
$f(v)$	activation function in ANN
G	mass velocity [kg/m^{2}s]
g	gravitational acceleration [m/s^2]
g_e	gravitational acceleration on Earth [m/s^2]
μg_e	microgravity [m/s^2]
H	height of channel's cross section [m]
h	enthalpy [J/kg]
h_{fg}	latent heat of vaporization [J/kg]
Ja^*	modified Jacob number, $c_{p,f}\Delta T_{sub,in}/h_{fg}$
j	superficial velocity [m/s]
L	length [m]
L_d	upstream development length of the FBM [m]
L_e	downstream exit length of the FBM [m]
L_h	heated length of FBM [m]
MAE	mean absolute error (%)
$\dot{m}$	mass flow rate [kg/s]
N	number of data points
N_{conf}	confinement number, $\{\sigma/g(\rho_f - \rho_g)D_h^2\}^{1/2} = Bd^{-1/2}$
n	mini-batch size in ANN
P_f	frictional perimeter of channel [m]
P_h	heated perimeter of channel [m]
p	pressure [Pa]
Δp	pressure drop [Pa]
p_{crit}	critical pressure of fluid [Pa]
p_r	reduced pressure, p/p_{crit}
q''	heat flux [W/m^2]
q''_{CHF}	critical heat flux [W/m^2]
$\%q$	percentage of heat flux [% of W/m^2]
Re	Reynolds number
r	Pearson's correlation coefficient
Su_{go}	vapor-only Suratman number, $\rho_g\sigma D_h/\mu_g^2$
T	temperature [°C]
ΔT_{sub}	fluid subcooling, $\Delta T_{sub} = T_{sat}$ - T_f [°C]
t	time [s]; target value in ANN
v	specific volume [m^3/kg]; weighted sum of inputs and bias at a neuron in ANN
v_{fg}	specific volume difference between liquid and vapor [m^3/kg]
W	width of channel's cross section [m]
We_{fo}	liquid-only Weber number, $G^2D_h/\sigma\rho_f$
w_i	weight in ANN
X	Lockhart-Martinelli parameter
x	flow quality
x_e	thermodynamic equilibrium quality, $(h - h_f)/h_{fg}$
x_i	input to ANN
y	output of ANN
z	streamwise coordinate [m]

Greek symbols

α	void fraction
β	channel aspect ratio, W/H
λ	dimensionless group in Lee and Lee correlation
μ	dynamic viscosity [kg/m.s]; mean in ANN
ξ_{30}	percentage of data predicted within ±30% of experimental value
ξ_{50}	percentage of data predicted within ±50% of experimental value
ρ	density [kg/m^3]
σ	surface tension [N/m]; standard deviation in ANN
ϕ	two-phase pressure drop multiplier
ψ	dimensionless group in Lee and Lee correlation
ω	parameter in Beattie and Whalley two-phase mixture viscosity model

Subscripts

A	accelerational component
e	equivalent
exp	experimental
F	frictional component
f	saturated liquid; single-phase liquid; bulk fluid
fo	liquid only
G	gravitational component
g	saturated vapor
go	vapor only
h	heated
i	index in ANN (= 1, 2, 3, …)
in	inlet to channel's heated section
k	index for a phase: liquid (f) or vapor (g)
out	outlet of channel's heated section
$pred$	predicted
sat	saturation
sb	saturated boiling
sc	subcooled boiling
sp	single-phase
tot	total
tp	two-phase
tt	turbulent-liquid turbulent-vapor
tv	turbulent-liquid laminar-vapor
vt	laminar-liquid turbulent-vapor
vv	laminar-liquid laminar-vapor
w	channel wall

Acronyms

ANN	Artificial Neural Network
CHF	Critical Heat Flux
FBCE	Flow Boiling and Condensation Experiment
FBM	Flow Boiling Module
GRC	NASA's Glenn Research Center
HEM	Homogeneous Equilibrium Model
ISS	International Space Station
nPFH	n-Perfluorohexane
ONB	Onset of Nucleate Boiling
PU-BTPFL	Purdue University Boiling and Two-Phase Flow Laboratory
SFM	Separated Flow Model

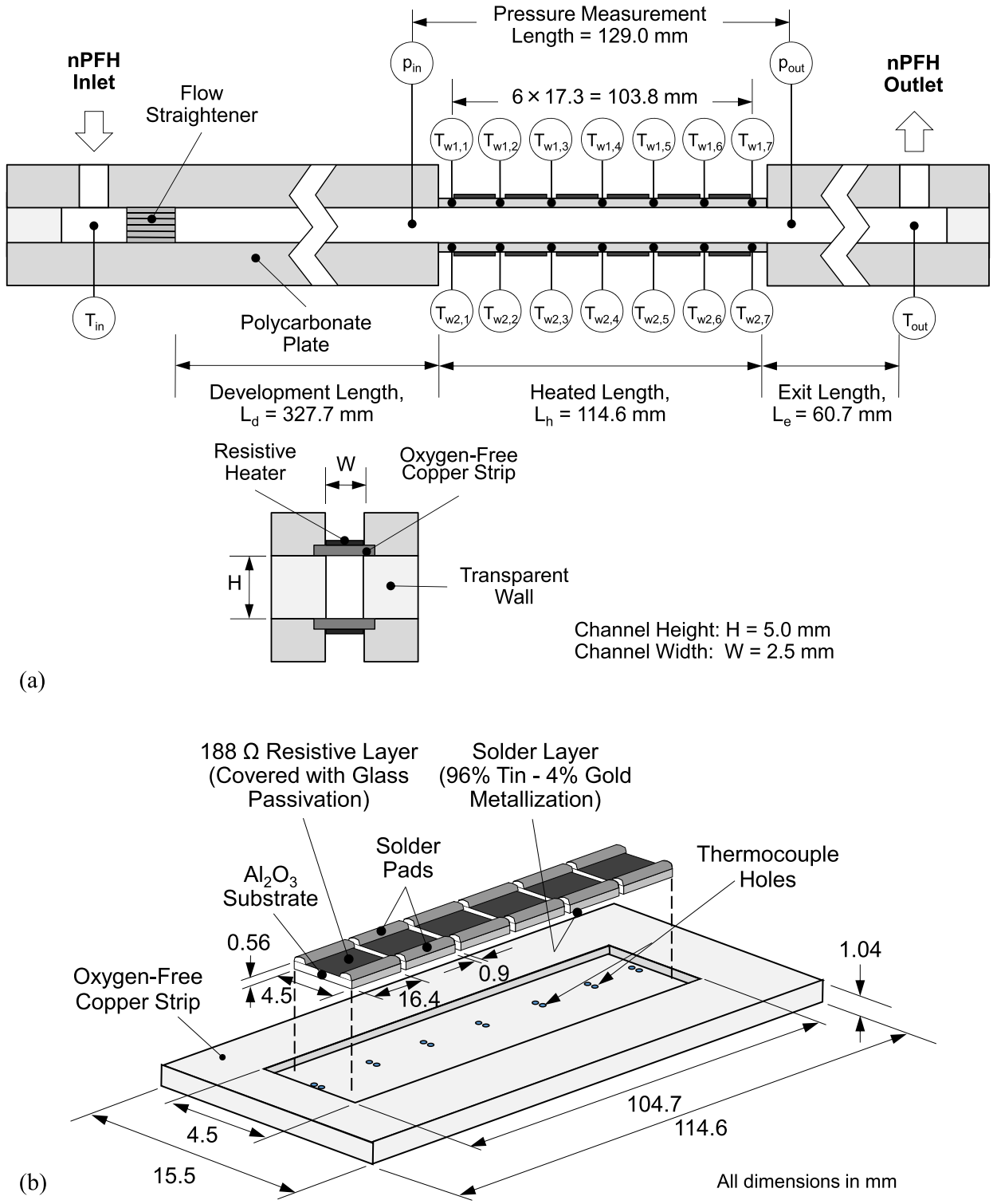

Fig. 1. Schematic diagrams of (a) the FBM including designation of temperature measurements and key dimensions and (b) the heated walls construction (adapted from [22,31]).

cooling schemes [8,9] has identified flow boiling as a prime contender for these applications. This is primarily due to the scheme's reliance on flow inertia – rather than body force – to supply the heated surfaces with fresh liquid for boiling. It can also handle high heat fluxes while meeting minimal size constraints, typically via cold plates.

1.2. Flow Boiling in Microgravity

The systems used in space missions experience a broad range of gravity levels, ranging from microgravity (μg_e) to hypergravity ($>1g_e$). This affects the thermal characteristics of flow boiling thermal management schemes, due to the very large difference in the densities of liquid and vapor phases. Several studies have focused on flow boiling in μg_e, often achieved in very short durations during free fall in drop towers

(*e.g.*, Ma and Chung [10]) and moderately longer durations onboard sounding/suborbital/ballistic rockets and parabolic flights (*e.g.*, Iceri *et al.* [11]). Drop towers offer a very good quality of μg_e, but the μg_e duration is too short for most experiments to reach steady state conditions [12]. Sounding rockets and parabolic flights offer longer μg_e durations, but the quality of μg_e is poor due to *g-jitter* (meaning, small fluctuations in μg_e level) [13], which artificially enhances heat transfer during experiments [14].

More recently, the International Space Station (ISS) [14–16] serves as a platform for performing boiling experiments in high quality μg_e over considerably longer durations and obtaining high quality μg_e data. Researchers in conjunction with the *Japanese Aerospace eXploration Agency* investigated flow boiling of n-Perfluorohexane (nPFH) in a copper and a glass heated tube onboard the ISS during 2017 – 2019. The research objectives of this *Two-Phase Flow Experiment* [17] and experimental heat loss estimates [18,19] have been reported. Another group in conjunction with the *European Space Agency* [20], aims to investigate flow boiling of nPFH in a copper tube, at much lower mass velocities of 20 – 150 kg/m^{2}s than the present study. An in-depth review of boiling experiments in μg_e is provided in the authors' prior article [21].

1.3. Flow Boiling and Condensation Experiment (FBCE)

FBCE is a long-term collaboration between researchers at PU-BTPFL and the NASA Glenn Research Center (GRC) to perform two-phase flow experiments in long-duration μg_e provided by the ISS. In early 2021, the FBCE system equipped with the Flow Boiling Module (FBM) underwent Mission Sequence Testing (MST) in Earth gravity. These MST experiments were performed for a subset of the ISS test matrix, and detailed results of both heat transfer and critical heat flux (CHF) were published for subcooled [22,23] and saturated inlet conditions [24]. Following the success of MST, in August 2021, the system was launched and installed on the ISS. During February – July 2022, the ISS flow boiling experiment matrix was remotely executed from GRC to obtain a substantial μg_e database. Heat transfer and interfacial flow physics aspects were presented in detail for both subcooled [21,25] and saturated inlet [26] with either one or two opposite walls heated. The CHF data was carefully analyzed and CHF mechanism, parametric trends, and predictive models and correlations were reported [27,28]. Consolidated databases consisting of data from both the ISS and Earth gravity experiments were used to develop new correlations for both subcooled flow boiling heat transfer [29] and CHF [30]. Further, a prediction tool for heat transfer and CHF using artificial neural networks was presented in [31]. These predictive tools have the capability to predict over broad ranges of operating conditions and different heating configurations and gravity levels.

With the heat transfer and interfacial flow aspects already investigated in detail over a series of studies, the next step is to study the pressure drop data collected during FBCE's ISS experiments.

1.4. Pressure Drop of Flow Boiling

Pressure drop (Δp) is an important parameter when it comes to designing and implementing thermal management systems. It is of great importance to develop prediction techniques for Δp, be it theoretical models, empirical correlations, or numerical simulations. Several tools are available for predicting Δp for flow boiling systems due to the relatively large magnitudes compared to traditional single-phase schemes. These are elaborated later in sections 4.2 for saturated flow boiling and 4.4 for subcooled flow boiling. However, the effectiveness of these tools in predicting Δp for μg_e flow boiling is not established. To assess the effectiveness of existing tools, as well as developing newer tools, a large μg_e database is necessary. The database amassed via FBCE's ISS experiments serves this purpose.

1.5. Objectives of Study

This study investigates Δp characteristics of μg_e flow boiling of nPFH introduced as either a subcooled liquid or a two-phase (liquid-vapor) mixture into a rectangular channel, that is heated along one wall or two opposite walls. The operating parameters of interest include mass velocity, inlet quality (or subcooling), inlet pressure, heat flux, and heated perimeter. The large database amassed is first used to elucidate parametric effects on Δp. Next, the capabilities of design tools, in the form of models and correlations, in predicting Δp are assessed and recommendations provided. Finally, a new artificial neural network is developed and shown to be an effective predictive tool for Δp.

2. Experimental Methods

A comprehensive writeup of experimental methods is provided in the authors' prior article [21]; only the most important aspects that pertain to the present study are described here. n-Perfluorohexane (nPFH, C_6F_{14}) is selected as the working fluid for its remarkable thermophysical properties that satisfy the requirements for space applications [32]. The thermophysical properties of nPFH are obtained from the NIST-REFPROP database [33].

2.1. Flow Boiling Module (FBM)

The FBM, schematics of which are shown in Fig. 1(a), is a highly instrumented test module test used to study various aspects of flow boiling as part of FBCE. It is constructed using three polycarbonate plates of thicknesses 25.15, 5.0, and 25.15 mm (in order) stacked together and clamped using aluminum braces. The flow channel is formed within the middle plate by milling a rectangular slot of 5.0 mm depth and 2.5 mm width, resulting in a hydraulic diameter of 3.33 mm. The flow channel consists of a 327.7 mm adiabatic development length, 114.6 mm heated length, and 60.7 mm adiabatic exit length, of which flow boiling only occurs within the middle heated length. The upstream and downstream adiabatic lengths, along with a honeycomb flow straightener, help straighten the flow streamlines within the heated length and lessen the effects of the 90° turn the nPFH takes both into and out of the FBM.

The channel is heated on two opposite sides, each by a copper heating strip of 114.6 mm length, 15.5 mm width, and 1.04 mm thickness, depicted in Fig. 1(b). Each heating strip is smooth on the nPFH heating side, and affixed to the other side are six thick-film resistive heaters. Each heater is 16.4 mm long, 4.5 mm wide, and 0.56 mm thick, and is comprised of an aluminum oxide substrate with a 188 Ω resistive layer between two solder pads. To provide a uniform surface heat flux, the heaters are wired in parallel and powered by direct current. The heaters are soldered to the copper strip to form a solder layer of 96% tin and 4% gold by composition. Each heater is recessed into the copper strip such that the thickness of copper between the heaters and the nPFH is 0.56 mm. In 0.9 mm gaps between each neighboring heater, type-E thermocouples are affixed to the strip within shallow hemispherical indentations, such that the distance between the thermocouple tip's center and the heating surface is 0.48 mm. Note that the heating strips are wider than the flow channel for O-ring sealing. Each strip can be independently powered to a maximum of 175 W, and the exact power can be determined from the voltage and current internally measured within a data acquisition system (DAQ).

The FBM is instrumented with absolute pressure transducers to measure the pressure at five locations: one close to the inlet, one close to the FBM outlet, and three within the development length. Of these, the pressures immediately upstream and downstream of the heated length are of utmost importance to this study and respectively designated p_{in} and p_{out}. The distance between p_{in} and p_{out} is 129.0 mm, of which 114.6 mm is heated and 14.4 mm is unheated. The FBM is also instrumented with type-E thermocouples extending into the flow to measure the bulk

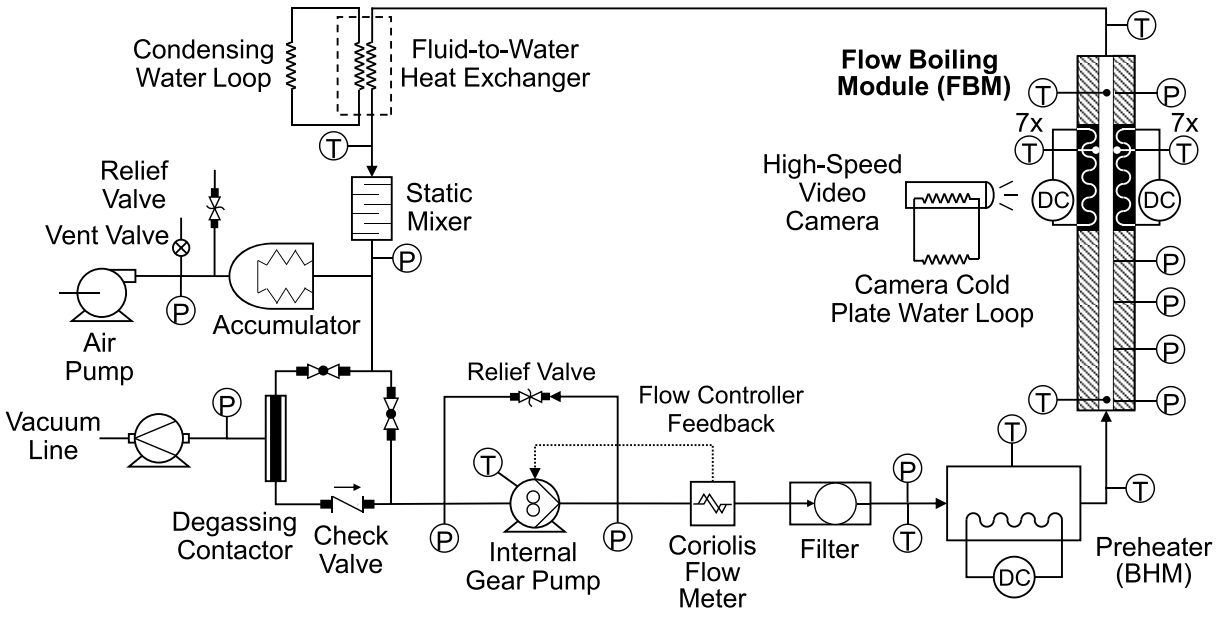

Fig. 2. Schematic diagram of the two-phase flow loop (adapted from [22]).

fluid temperatures near the inlet and outlet, which are respectively designated T_{in} and T_{out}.

2.2. Two-Phase Flow Loop

The experiments utilize a closed flow loop, shown in the schematics in Fig. 2, to deliver the nPFH at the conditions required at the inlet of the FBM. Subcooled nPFH is forced through the loop by a gear pump. The set flow rate is maintained by a flow controller, which takes feedback from a Coriolis flow meter downstream of the pump. The temperature and flow quality of the nPFH at the FBM inlet is achieved by an upstream preheater (also known as the Bulk Heater Module, BHM). After entering the FBM, the nPFH boils and a two-phase mixture exits to enter a fluid-to-water heat exchanger serving as the condenser in the loop. The exiting subcooled nPFH passes through a static mixer, and then re-enters the pump. The nPFH is stored in an accumulator connected to the flow loop, and this helps both maintain the operating pressure desired within the loop and mitigate two-phase flow instabilities [34]. The purity of nPFH is ensured by a degassing process that uses a membrane contactor at regular intervals prior to each set of experimental cases.

As indicated in Fig. 2, the flow loop is instrumented with absolute pressure transducers and thermocouples/RTDs to measure the pressure and temperature at several locations. The Coriolis flow meter measures the mass flow rate of nPFH. All sensor measurements are read by 2 DAQs and a continuous temporal record is saved at 5 Hz sampling rate during experiments.

Table 1
Summary of key parameters of the ISS μg_e flow boiling database (for $\Delta p > 1.4$ kPa).

Parameter	Value
Fluid	nPFH
Environment	Microgravity (μg_e)
Channel heating configuration	Single-sided, Double-sided
Mass flow rate, $\dot{m}$	2.25 – 40.0 g/s
Mass velocity, G	180.0 – 3200.1 kg/m^{2}s
Inlet pressure, p_{in}	119.6 – 200.4 kPa
Inlet saturation temperature, $T_{sat,in}$	62.1 – 78.9°C
Inlet temperature, T_{in}	23.0 – 80.8°C
Inlet subcooling, $\Delta T_{sub,in}$	0.0 – 46.0°C
Inlet quality, x_e	-0.62 – 0.87
Wall heat flux, q''_w	< 55.1 W/m^2
Pressure drop, Δp	1.40 – 21.5 kPa

2.3. Experiment Summary and Data Processing

Lists of ISS experiments with subcooled inlet are provided in [21,25] and two-phase inlet in [26] with the respective operating conditions; the experimental reference numbers (Expt.#) correspond to the tables provided within, and enable easy cross-referencing to the raw data made available in a NASA repository. Each experiment is performed by setting the inlet conditions, including mass velocity, G, inlet pressure, p_{in}, and inlet thermodynamic equilibrium quality, $x_{e,in}$. For each set of conditions, heat flux is incremented from a minimum level to CHF in a discrete stepwise fashion with 120 – 180 seconds for each step. The last 20 seconds of temporal data for each step is averaged to obtain each steady state datapoint.

Heat losses both upstream of and within the FBM is already quantified in the author's prior articles [21,26], and they are incorporated within the heat fluxes and fluid enthalpies reported in this study. For subcooled inlet, enthalpy at the FBM inlet, h_{in}, is directly referenced from REFPROP, whereas for two-phase inlet, h_{in} is derived from the enthalpy at the BHM inlet (where the fluid is always a highly subcooled liquid) after incorporating upstream heat losses. Enthalpy at the FBM outlet is determined as

$$h_{out} = h_{in} + \frac{q''_w P_h L_h}{\dot{m}}, \tag{1}$$

where q''_w is FBM heat flux and P_h is heated perimeter. $P_h = W = 2.5$ mm for single-sided heating and $P_h = 2W = 5$ mm for double-sided, where W is the channel width. The frictional perimeter is $P_f = 15$ mm. Thermodynamic equilibrium qualities at the FBM's inlet and outlet are calculated as

$$x_e = \frac{h - h_f|_p}{h_{fg}|_p}, \tag{2}$$

where h is local enthalpy and both h_f saturated liquid enthalpy and h_{fg} latent heat of vaporization are evaluated at local pressure.

Pressure drop of the FBM's heating length is determined from the absolute pressure measurements as

$$\Delta p = p_{in} - p_{out}. \tag{3}$$

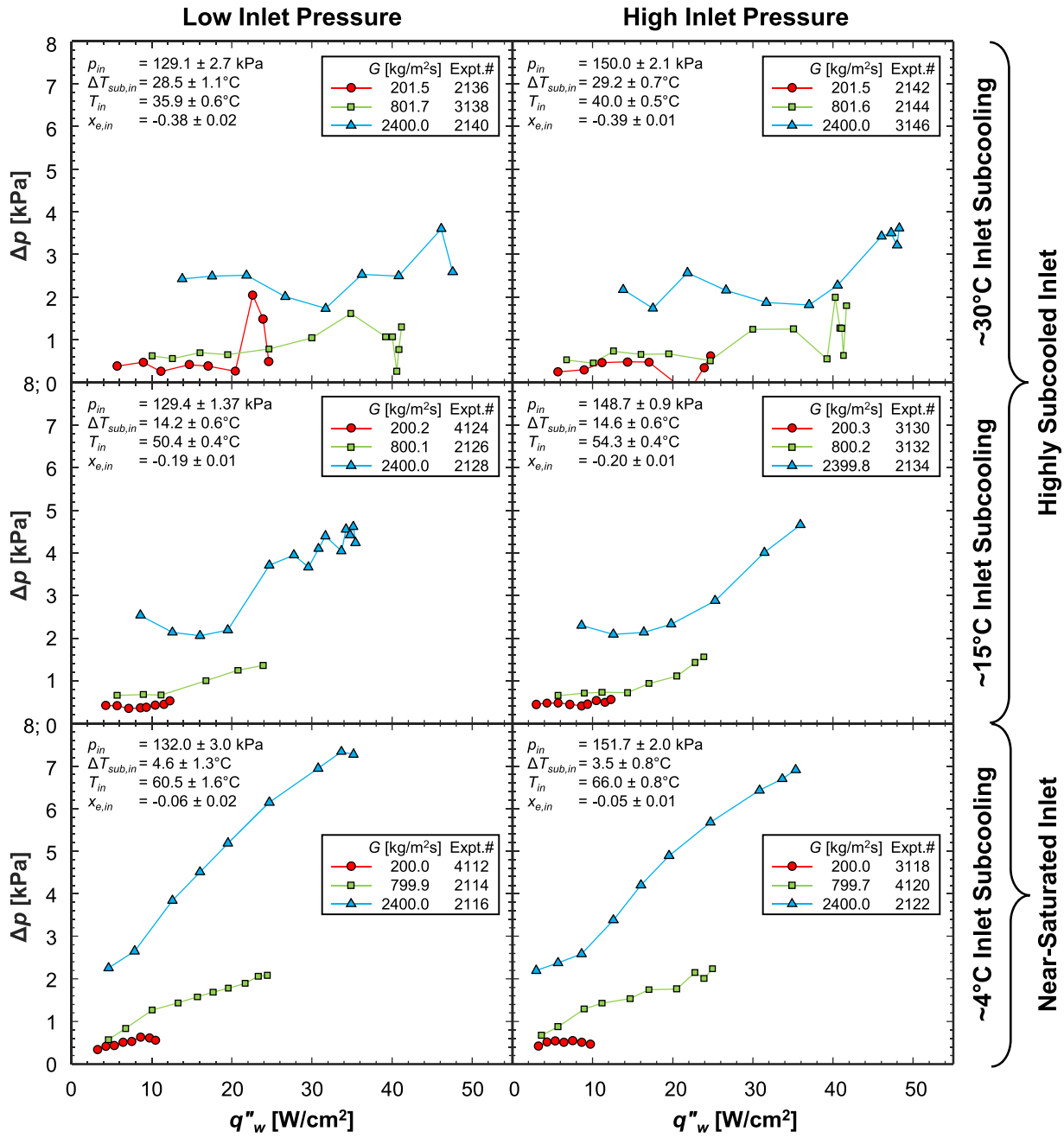

Fig. 3. Variations of pressure drop, Δp, with single-side-heated wall heat flux, q''_w, for three mass velocities at six different inlet conditions (three inlet subcoolings × two inlet pressures). Exact operating conditions (inlet pressure, p_{in}, inlet temperature, T_{in}, inlet subcooling, $\Delta T_{sub,in}$, and inlet quality, $x_{e,in}$) for the data in each plot are provided within the corresponding plot. Within each plot, each curve pertains to a different mass velocity in the range of $G \approx 200 - 2400$ kg/m^{2}s.

Note that experimental Δp embodies a relatively small unheated length, which is considered in further modeling. Absolute pressure measurement has a maximum uncertainty of ±0.7 kPa, so Δp has a maximum uncertainty of ±1.4 kPa. Experimental datapoints with $\Delta p <$ 1.4 kPa were excluded from further modeling and analyses (sections 4 and 5 of this study) in order to avoid large errors associated with uncertainty (this reduced the number of datapoints from 3393 to 2478). Maximum measurement uncertainty for temperature is ±0.5°C, FBM heater power is ±0.3%, preheater power is ±0.6%, and mass flow rate is ±0.6% of reading. Overall, a summary of key parameters of the ISS μg_e flow boiling database is given in Table 1.

3. Pressure Drop Characteristics of Microgravity Flow Boiling onboard the ISS

The primary operating parameters explored in this study include mass velocity (G), inlet subcooling ($\Delta T_{sub,in}$) or inlet quality ($x_{e,in}$, which significantly varies from highly subcooled to saturated liquid-vapor mixture inlet), inlet pressure (p_{in}, which affects thermophysical properties), and wall heat flux (q''_w).

3.1. Steady-State Parametric Effects for Flow Boiling with Subcooled Inlet

Variations of pressure drop, Δp, with q''_w are included in Fig. 3 for single-sided heating and subcooled inlet. Six plots are presented, each corresponding to a different set of inlet conditions (three inlet

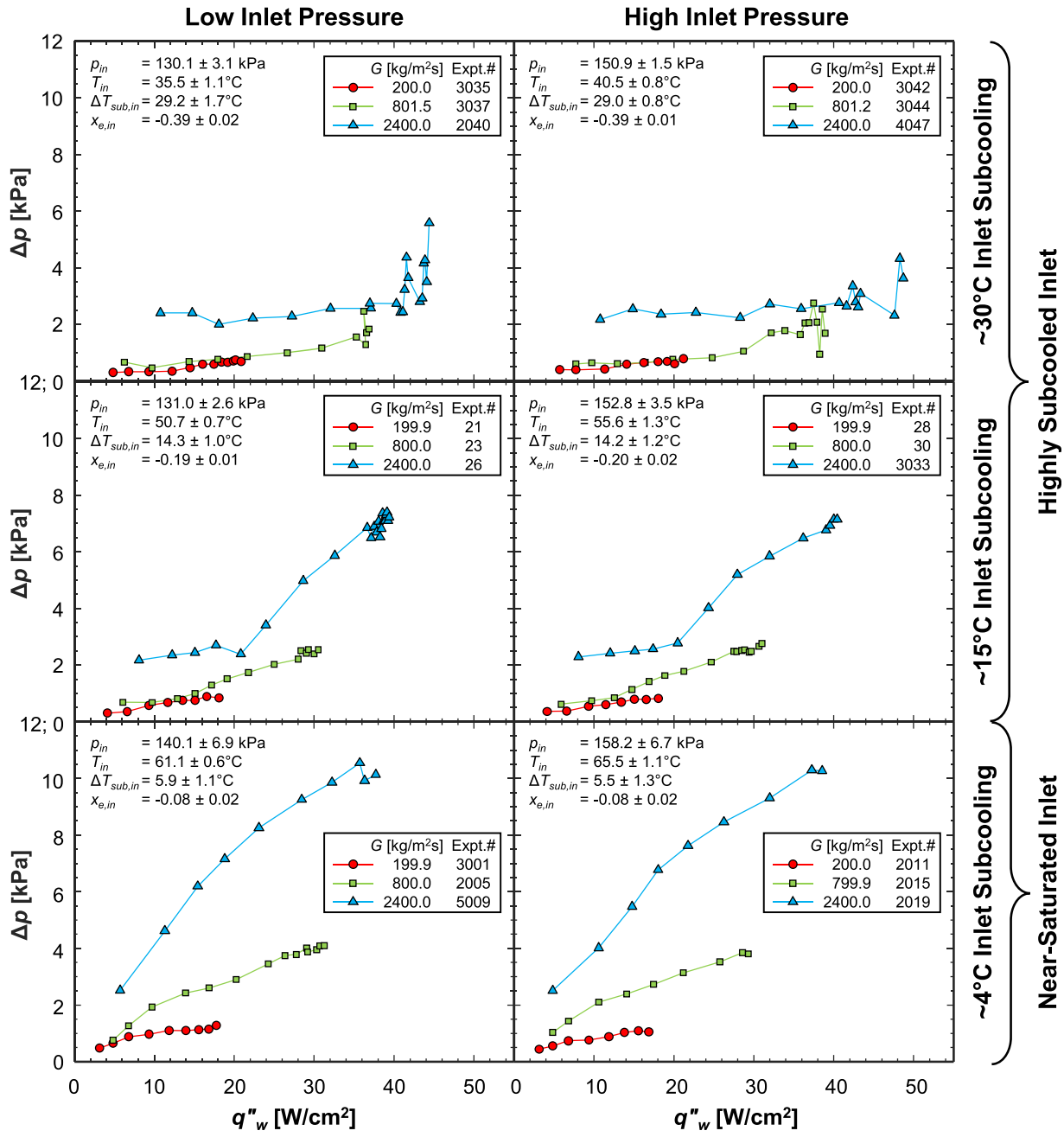

Fig. 4. Variations of pressure drop, Δp, with double-side-heated wall heat flux, q''_w, for three mass velocities at six different inlet conditions (three inlet subcoolings × two inlet pressures). Exact operating conditions (inlet pressure, p_{in}, inlet temperature, T_{in}, inlet subcooling, $\Delta T_{sub,in}$, and inlet quality, $x_{e,in}$) for the data in each plot are provided within the corresponding plot. Within each plot, each curve pertains to a different mass velocity in the range of $G \approx 200 - 2400$ kg/m^{2}s.

subcoolings × two inlet pressures). Within each plot, each curve pertains to a different G in the range of 200 – 2400 kg/m^{2}s. Some overall physical trends include:

(i) Δp increases upon increasing q''_w. This is due to the increased amount of vapor production, accelerating the flow to higher bulk flow velocities, which yield large frictional and accelerational components of Δp. This increase is more significant for near-saturated inlet (plots in the bottom row) because the flow easily transitions to saturated boiling, where the condensing potential of the bulk flow is negligible. This means the produced vapor remains intact, without condensing back to liquid, resulting in significantly high void fractions and therefore high local fluid velocities. On the other hand, for highly subcooled inlet, the flow has a strong condensing potential, so the produced vapor partially condenses back to liquid, resulting in low void fractions, low fluid velocities, and low Δp.

(ii) The Δp curves are higher for high G and Δp monotonically increases upon increases in G. This is attributed to both frictional and accelerational components of Δp being high at high flow velocities.

(iii) The slope of Δp versus q''_w increases upon increasing G, indicating the combined contribution of G and q''_w in building up Δp. This is apparent especially for near-saturated inlet, where the produced vapor remains intact and higher G combined with flow acceleration results in enormously high flow velocities.

(iv) There are no discernible differences between the trends for low (~130 kPa) and high (~150 kPa) inlet pressures, due to

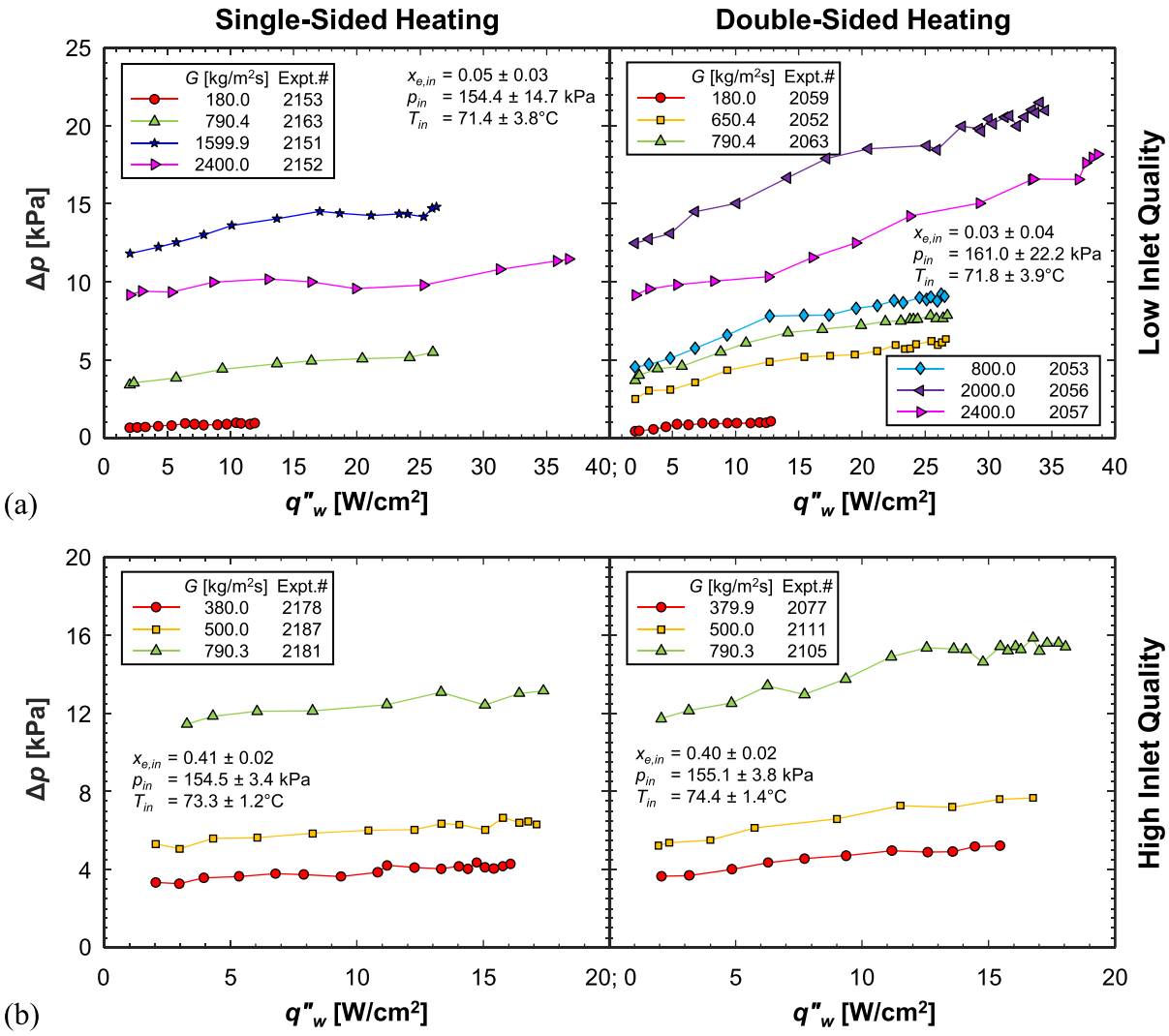

Fig. 5. Variations of pressure drop, Δp, versus wall heat flux, q''_w, for different mass velocities, G, with single- and double-sided heating at (a) low and (b) high inlet qualities, $x_{e,in}$. Exact operating conditions (inlet quality, $x_{e,in}$, inlet pressure, p_{in}, and inlet temperature, T_{in}) for the data in each plot are provided within the corresponding plot.

unappreciable variations in thermophysical properties at this pressure range.

(v) Most Δp curves, particularly those with highly subcooled inlet and high q''_w, are jagged with some sharp peaks and troughs. This is due to the manifestation of severe two-phase flow instabilities at these operating conditions, which are further elaborated in section 3.3.

Similar plots are presented for double-sided heating in Fig. 4 with an identical layout and choice of operating conditions. The parametric trends already observed for single-sided heating in Fig. 3 still hold, meaning they are independent of heating configuration. Comparing single- and double-sided heating, higher heating area at identical heat fluxes result in higher Δp due to a larger amount of heat resulting in larger void fractions and increased flow acceleration.

3.2. Steady-State Parametric Effects for Flow Boiling with Saturated Inlet

Plots showing variations of Δp versus q''_w for different G are included in Fig. 5 for saturated inlet with both single- and double-sided heating. At low inlet qualities of $x_{e,in} \approx 0.04$, shown in Fig. 5(a), Δp monotonically increases upon increasing G at all heat fluxes. The one anomaly seems to be the Δp curve for $G = 2400$ kg/m^{2}s lies below that for 1600 kg/m^{2}s and 2000 kg/m^{2}s during single- and double-sided heating, respectively. This reduced Δp is probably due to reduced phase change and acceleration effects, despite the mass flow being high at the inlet. On a typical N-shaped curve of Δp versus G for flow boiling, $G = 2400$ kg/m^{2}s could fall on the downward-slope portion while the lower G fall on the positive-slope portion. The curves are smoother than those for subcooled inlet because two-phase flow instabilities are less prominent at saturated conditions in μg_e. Upon increasing heat flux, Δp monotonically increases due to increased void fraction within the channel. Double-sided heating is characterized by higher Δp due to doubling of the amount of vapor and higher flow velocities. At high inlet qualities of $x_{e,in} \approx 0.40$, shown in Fig. 5(b), similar physical trends apply. Compared to low $x_{e,in}$, for high $x_{e,in}$, Δp does not increase to a considerable extent upon increasing q''_w, due to (i) very high void fractions introduced into the channel, so the flow velocity is very high for a fixed G, and (ii) CHF occurs at lower heat fluxes, so the flow can accommodate a lower amount of heat addition (note the curves extend until CHF).

Plots presenting variations of Δp versus q''_w for different $x_{e,in}$ are included in Fig. 6 for saturated inlet with both single- and double-sided heating. Respectively arranged from the top to bottom are plots for $G =$ 380, 500, and 790 kg/m^{2}s. Δp monotonically increases upon increasing $x_{e,in}$ owing to high flow velocities resulting from increased vapor fractions entering the channel. Although Δp increases with increasing q''_w, a

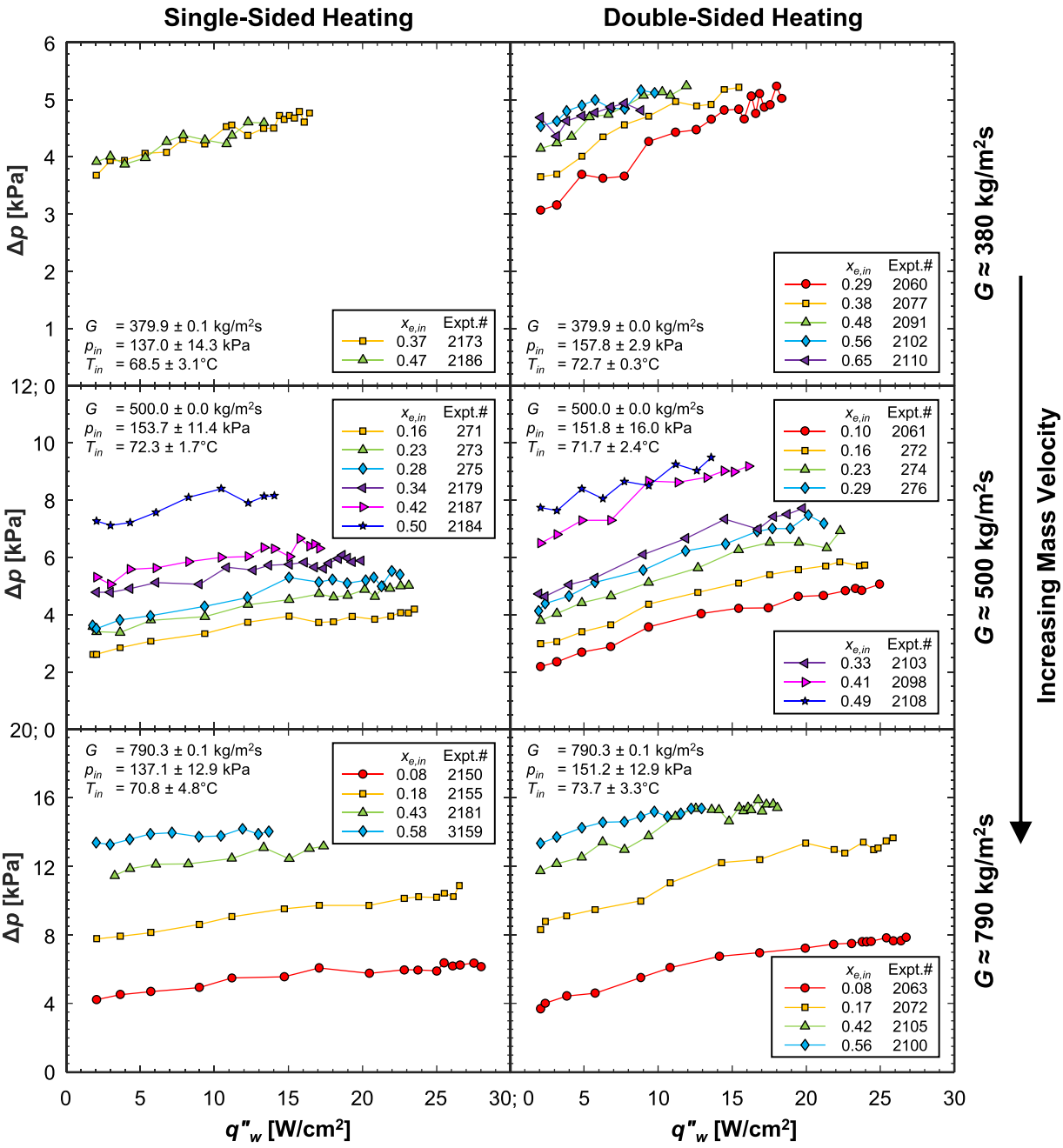

Fig. 6. Variations of pressure drop, Δp, versus wall heat flux, q''_w, for different inlet qualities, $x_{e,in}$, at six combinations of operating conditions and heating configuration: mass velocity, G, is increasing from the top to bottom plot, and single- and double-sided heating are respectively on the left and right. Exact operating conditions (inlet quality, $x_{e,in}$, inlet pressure, p_{in}, and inlet temperature, T_{in}) for the data in each plot are provided within the corresponding plot.

plateauing effect is seen beyond a particular q''_w for each curve; this is apparent in the curves at higher G. The highest Δp is obtained at a combination of highest G, highest $x_{e,in}$, highest q''_w with double-sided heating.

3.3. Temporal Δp Characteristics during Two-Phase Flow Instabilities

Microgravity flow boiling is prone to dynamic two-phase flow instabilities, especially at certain combinations of operating conditions (such as high heat flux and high subcooling). This aspect has been studied in detail by the present authors in [35]. Instabilities induce severe periodic oscillations in inlet pressure and Δp in the flow system. A representative case is shown in Fig. 7, where instabilities were observed for $G = 803.6$ kg/m^{2}s, $\Delta T_{sub,in} = 28.9$°C, and $q''_w = 34.6$ W/cm^2 = 80.5% q''_{CHF} in μg_e. Respectively shown at the top and bottom of Fig. 7(a) are temporal plots of p_{in} and Δp over a 20 second data averaging period to obtain a single steady-state datapoint. p_{in} oscillations are severe and span over a range of ~110 – 180 kPa, averaging 147.7 kPa. Likewise, Δp oscillations are severe and span over a range of about -10 – 12 kPa, averaging 1.1 kPa. A short subset of the time period is plotted in Fig. 7 (b). p_{in} oscillations are clear and regular over the time period, whereas Δp oscillations seem irregular, probably due to a need for higher sampling frequencies to capture the oscillations. The corresponding flow image sequence, tracking the motion of interfacial feature, is shown in Fig. 7(c). The flow direction is from the bottom to top, while the channel is heated along the left wall. Red arrowheads are used to track certain distinct features, and the time stamp of each image is provided underneath it. The image sequence shows nucleation in the channel's

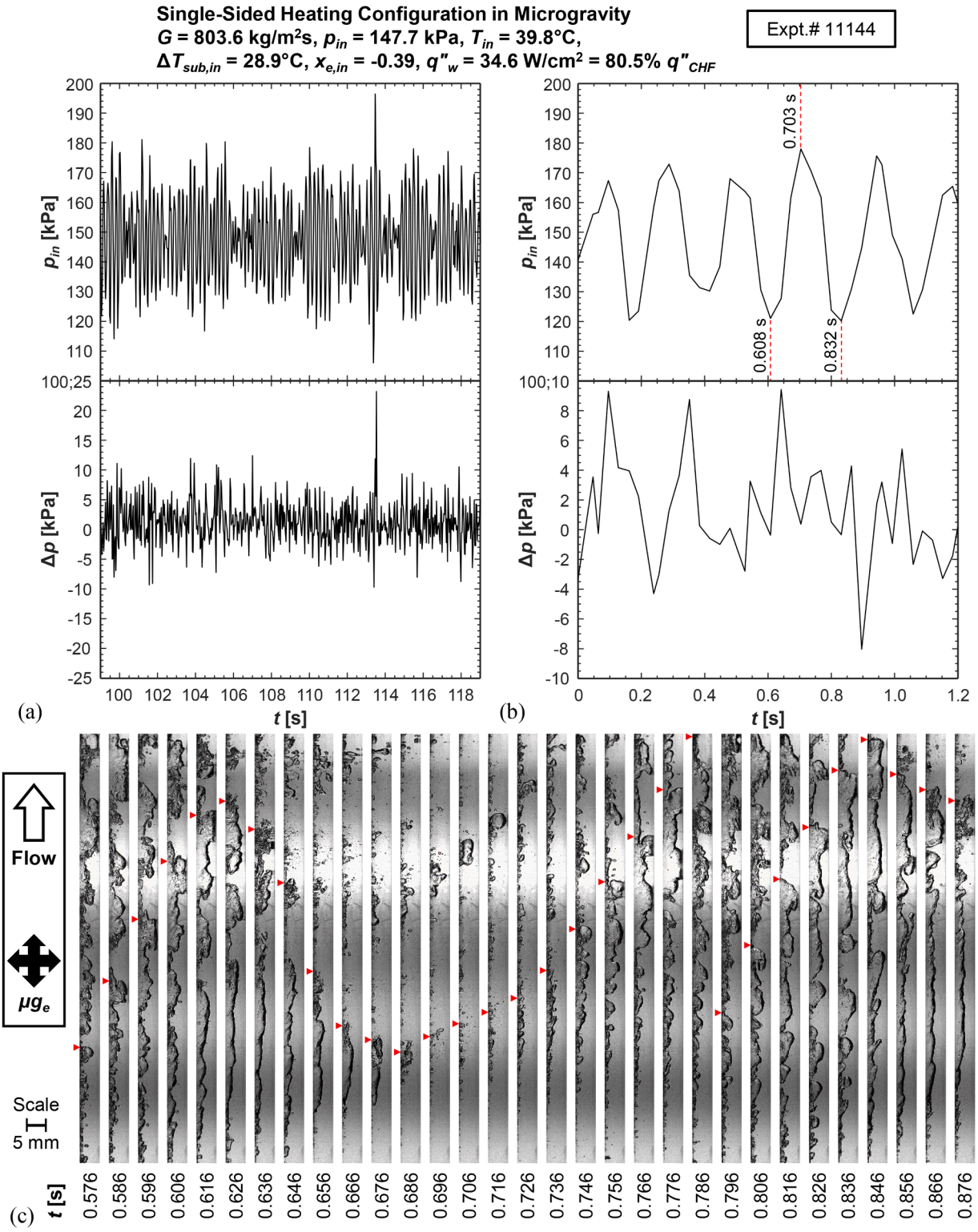

Fig. 7. Flow instabilities during a mass velocity of $G = 803.6$ kg/m^{2}s, inlet subcooling of $\Delta T_{sub,in} = 28.9$°C, and heat flux of $q''_w = 34.6$ W/cm^2 = 80.5% q''_{CHF} in microgravity. Temporal plots of inlet pressure and pressure drop over the (a) 20 second data averaging period and (b) a shorter period within. (c) Corresponding flow image sequence tracking motion of interfacial features with time stamps.

upstream region and a rather significant thickening of the vapor layer towards the downstream region. At $t = 0.576$ s, a trough of the wavy liquid-vapor interface is tracked around a third of the channel length from the inlet. Flow is in the forward direction until 0.626 s, after which the tracked feature moves against the streamwise direction because of liquid backflowing into the channel, bulk flow reversing, and the produced vapor within the channel condensing back to liquid. This occurs shortly after the p_{in} minimum at 0.608 s. At 0.686 s, the flow once again changes direction forward, which roughly corresponds to a maximum of p_{in}. A second surge of backflow is observed at 0.846 s, roughly making the duration to this backflow oscillation to be 0.22 s. The corresponding p_{in} oscillations occur with a similar period and a

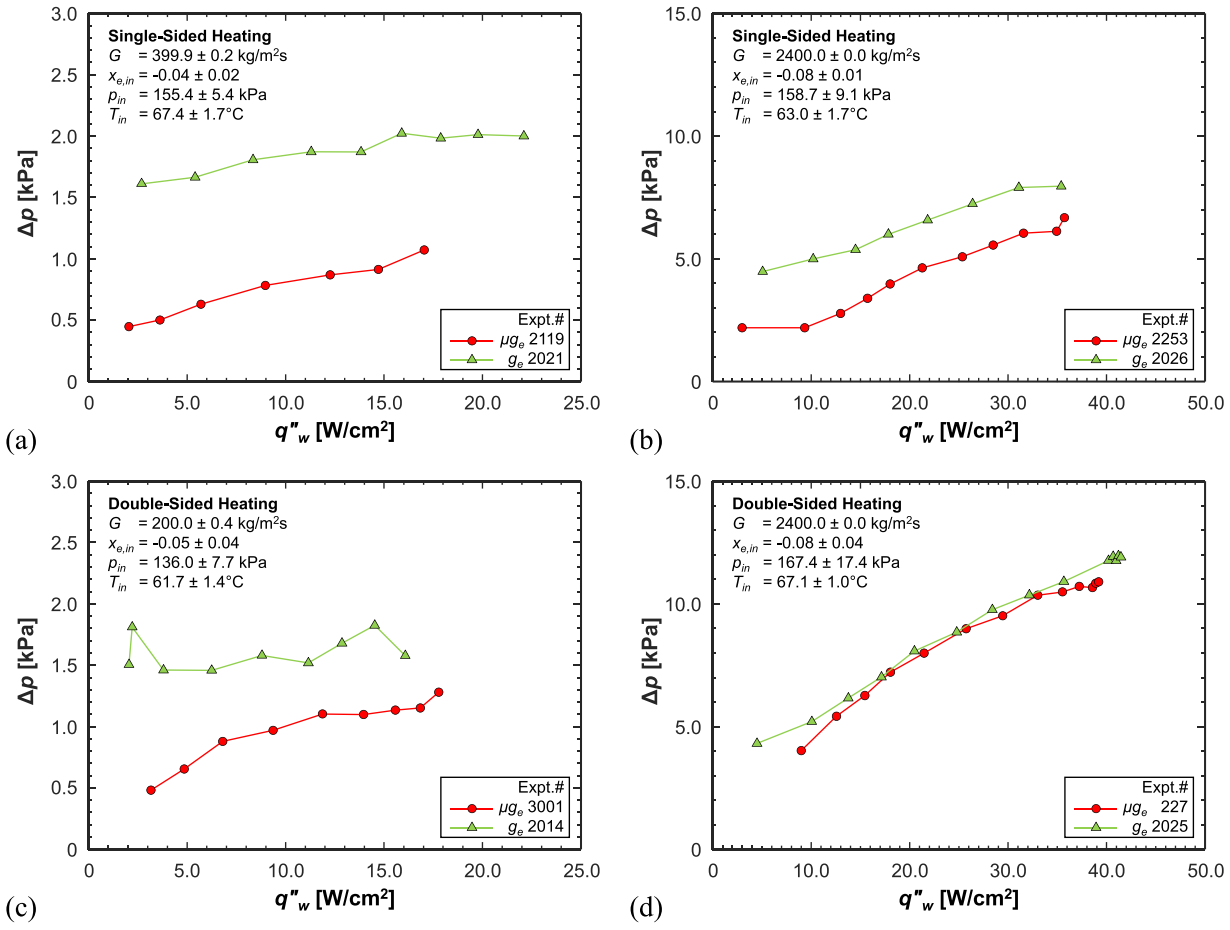

Fig. 8. Comparison of pressure drop, Δp, in microgravity, μg_e, to vertical upflow in Earth gravity, g_e, during single-sided heating with a mass velocity of (a) $G \approx 400$ and (b) 2400 kg/m^{2}s and double-sided heating with (c) $G \approx 200$ and (b) 2400 kg/m^{2}s.

frequency of 4-5 Hz.

3.4. Comparison to Vertical Upflow in Earth Gravity

As referenced in section 1.3, a final set of ground tests called Mission Sequence Testing (MST) was performed prior to the FBCE system's launch to the ISS. MST consisted of a subset of the test matrix performed onboard the ISS, generally the extreme operating conditions, but during vertical upflow in g_e. Fig. 8 presents plots comparing measured Δp in μg_e to those obtained during MST at similar operating conditions. Figs. 8(a-d) show plots for single-sided heating at mass velocities of $G \approx 400$ and 2400 kg/m^{2}s, and double-sided heating at $G \approx 200$ and 2400 kg/m^{2}s, respectively. Δp in μg_e is consistently lower than that during vertical upflow in g_e because gravity opposes vertical upflow and increases total pressure drop. For each set of operating conditions, the difference between Δp for μg_e and g_e vertical upflow decreases as q''_w increases, due to greater vapor production within the channel. Increased vapor production increases the accelerational component of pressure drop and decreases the density of the two-phase mixture, reducing the influence of the gravitational component on total pressure drop. In a similar vein, the additional vapor production during double-sided heating compared to single-sided at the same q''_w decreases the difference between total Δp for μg_e and g_e vertical upflow. Double-sided heating at $G \approx 2400$ kg/m^{2}s, shown in Fig. 8(d), results in the highest Δp, but nearly identical Δp in μg_e and vertical upflow in g_e. The combination of double-sided heating and high mass velocity increases the frictional and accelerational component of Δp, and the impact of the gravitational component of Δp is negligible.

4. Conventional Prediction Techniques for Flow Boiling Pressure Drop

4.1. Overview

Conventionally, Δp for flow boiling is determined using a consolidation of Δp relations, models, and correlations. For example, consolidated predictive methods for flow boiling in microchannel heat sinks was developed in [36] and annuli in [37]. Flow boiling generally consists of several heat transfer regimes along the streamwise direction. If the channel is supplied with subcooled liquid at its inlet, the first upstream regime will be single-phase liquid convection. Downstream of the onset of nucleate boiling (ONB) location, subcooled flow boiling will occur with $x_e < 0$. Starting at the location where the bulk fluid attains saturation, $x_e \geq 0$, lies the saturated flow boiling regime. In case the particular application allows for complete liquid evaporation, so $x_e \geq 1$, single-phase vapor convection will occur close to the channel exit. Either all or some of these regimes will manifest in a given flow boiling scenario, and their presence depends on the combination of fluid, operating conditions, and geometrical parameters. For example, depending on the channel length, the fluid could exit in a subcooled, saturated, or superheated state.

Total pressure drop in the channel, Δp_{tot}, is the summation of the Δp of each individual regime present; in general, Δp_{tot} = (single-phase liquid pressure drop, $\Delta p_{sp,f}$) + (two-phase subcooled boiling drop, Δp_{sc}) + (two-phase saturated boiling drop, Δp_{sb}) + (single-phase vapor pressure drop, $\Delta p_{sp,g}$). Typically, the flow channel is divided into several streamwise segments and pressure is marched forwards using appropriate relations based on the local regime. For accurate Δp predictions,

each individual model/correlation for each regime must be accurate. Δp relations for the single-phase regimes are theoretically derived and are proportional to Fanning friction factor, f, for which several relations are available in the literature, typically segregated based on Reynolds number. Research has matured to a point that no doubt exists on the accuracy of these f relations for the flow conditions in this study. However, Δp predictions for subcooled and saturated flow boiling, especially in μg_e, still has several questions on the applicability of seminal correlations and models (which were developed based on $1g_e$ data).

An assessment is made to determine the effectiveness of conventional two-phase Δp predictive tools for saturated flow boiling in μg_e in sections 4.2-4.3 and subcooled flow boiling in μg_e in sections 4.4-4.5. The assessment method assumes the flow to be steady and does not consider any two-phase instabilities that cause dynamic flow oscillations [34]. The channel is divided into 645 streamwise segments of equal lengths and calculations are performed in a one-dimensional fashion ignoring both gravity and any variations across the channel's cross section. Thermophysical properties are estimated based on local fluid temperature (equal to saturation temperature within the saturated boiling regime). Local quality, x_e, is estimated based on inlet quality, $x_{e,in}$, and energy balance over the channel considering uniform heat addition from each heated wall.

$$f_{tp}=\begin{cases}24\left(\begin{matrix}1-1.3553\beta+1.9467\beta^2-1.7012\beta^3\\+0.9564\beta^4-0.2537\beta^5\end{matrix}\right)Re_{tp}^{-1}, & Re_{tp}<2000\\ 0.079Re_{tp}^{-0.25}, & 2000\le Re_{tp}<20000\\ 0.046Re_{tp}^{-0.2}, & Re_{tp}\ge 20000\end{cases} \tag{9}$$

The prediction performance of each seminal model/correlation is assessed by comparing the predicted pressure drop, Δp_{pred}, with experimentally measured values, Δp_{exp}, for the entire μg_e database. Statistical measures in terms of Mean Absolute Error for N datapoints,

$$MAE=\frac{1}{N}\sum_{N}\frac{\left|\Delta p_{pred}-\Delta p_{\exp}\right|}{\Delta p_{\exp}}\times 100\%, \tag{4}$$

and percentages of datapoints predicted within ±30% and ±50%, ξ_{30} and ξ_{50}, respectively, are used to determine the predictive accuracy.

4.2. Pressure Drop for Saturated Flow Boiling

Total pressure drop for the saturated flow boiling regime, Δp_{sb}, is given by the summation of frictional, accelerational, and gravitational components as

$$\Delta p_{sb}=\Delta p_{sb,F}+\Delta p_{sb,A}+\Delta p_{sb,G}. \tag{5}$$

Frictional pressure gradient is determined using two classical models: the Homogeneous Equilibrium Model (HEM) and the Separated Flow Model (SFM). Accelerational pressure gradient is evaluated using a theoretical equation,

$$-\left(\frac{dp}{dz}\right)_A=G^2\frac{d}{dz}\left[\frac{v_g x^2}{\alpha}+\frac{v_f(1-x)^2}{(1-\alpha)}\right], \tag{6}$$

with void fraction, α, estimated using appropriate techniques for HEM and SFM. Since the flow is in μg_e, gravitational Δp is negligible.

4.2.1. Homogeneous Equilibrium Model

The HEM considers the saturated two-phase mixture as a pseudo single-phase fluid that obeys simple mass, momentum, and energy conversation equations, but with properties intermediary between those of the liquid and vapor. The HEM assumes (i) the flow quality, x, to be equal to the thermodynamic equilibrium quality, x_e, (ii) only latent heat transfer occurs between the two phases, (iii) the velocity of the two phases is equal with a uniform profile across each phase, and (iv) both pressure and mixture properties are uniform across the flow cross-section. Void fraction is estimated from flow quality (equal to thermodynamic equilibrium quality for saturated boiling) as

$$\alpha=\left[1+\left(\frac{1-x_e}{x_e}\right)\left(\frac{v_f}{v_g}\right)\right]^{-1}. \tag{7}$$

Frictional pressure gradient is given by a simple theoretical relation,

$$-\left(\frac{dp}{dz}\right)_F=\frac{2f_{tp}\,v_f\,G^2}{D_h}\left(1+x_e\frac{v_{fg}}{v_f}\right), \tag{8}$$

where two-phase friction factor is determined for rectangular channels of aspect ratio, $\beta = W/H$, as

Two-phase Reynolds number, defined as

$$Re_{tp}=\frac{GD_h}{\mu_{tp}}, \tag{10}$$

is dependent on two-phase mixture viscosity, μ_{tp}. Several relations for μ_{tp} exist in the literature [38–45], and those assessed in this study are listed in Table 2. Among these, the relations by McAdams *et al.* [38], Cicchitti *et al.* [40], Dukler *et al.* [42,43], Beattie and Whalley [44], and Lin *et al.* [45] satisfy the limiting conditions of $\mu_{tp}=\mu_f$ at $x_e=0$ and $\mu_{tp}=\mu_g$ at $x_e=1$, while those by Akers *et al.* [39] and Owens [41] do not.

4.2.2. Separated Flow Model

The SFM considers the saturated two-phase mixture as two discrete phases that are separated from each other, with each having its own properties and velocities [46]. Void fraction is estimated using the widely-applicable correlation by Zivi [47],

$$\alpha=\left[1+\left(\frac{1-x_e}{x_e}\right)\left(\frac{v_f}{v_g}\right)^{2/3}\right]^{-1}. \tag{11}$$

Frictional pressure drop, $\Delta p_{sb,F}$, is estimated by the Lockhart-Martinelli method [48], where frictional pressure gradient is expressed as the product of the frictional pressure gradient of one of the phases and a two-phase multiplier, ϕ_k,

$$-\left(\frac{dp}{dz}\right)_F=\begin{cases}-\left(\frac{dp}{dz}\right)_{Ff}\phi_f^2, & -\left(\frac{dp}{dz}\right)_{Ff}\phi_f^2>-\left(\frac{dp}{dz}\right)_{Fg}\phi_g^2\\ -\left(\frac{dp}{dz}\right)_{Fg}\phi_g^2, & -\left(\frac{dp}{dz}\right)_{Fg}\phi_g^2>-\left(\frac{dp}{dz}\right)_{Ff}\phi_f^2\end{cases}. \tag{12}$$

The phase-specific frictional pressure gradient is expressed as

$$-\left(\frac{dp}{dz}\right)_{Ff}=\frac{2f_f\,G^2(1-x_e)^2v_f}{D_h}\ \text{for liquid, and} \tag{13}$$

$$-\left(\frac{dp}{dz}\right)_{Fg}=\frac{2f_g\,G^2x_e^2\,v_g}{D_h}\ \text{for vapor,} \tag{14}$$

where the friction factors are given for any phase k (= f for liquid and g for vapor) as

$$f_k = \begin{cases} 24\left(\begin{matrix}1 - 1.3553\beta + 1.9467\beta^2 - 1.7012\beta^3 \\ +0.9564\beta^4 - 0.2537\beta^5\end{matrix}\right) Re_k^{-1}, & Re_k < 2000 \\ 0.079 Re_k^{-0.25}, & 2000 \le Re_k < 20000 \\ 0.046 Re_k^{-0.2}, & Re_k \ge 20000 \end{cases} \quad (15)$$

The phase-specific Reynolds numbers are given as

$$Re_f = \frac{(1 - x_e)\, G D_h}{\mu_f} \text{ for liquid, and} \quad (16)$$

$$Re_g = \frac{x_e G D_h}{\mu_g} \text{ for vapor.} \quad (17)$$

ϕ_k is typically a function of Lockhart-Martinelli parameter, X, and empirical constant, C, as

$$\phi_f^2 = 1 + \frac{C}{X} + \frac{1}{X^2} \text{ for liquid, and} \quad (18)$$

$$\phi_g^2 = 1 + CX + X^2 \text{ for vapor,} \quad (19)$$

where X is defined as

$$X = \left[-\left(\frac{dp}{dz}\right)_{F,f} \Big/ -\left(\frac{dp}{dz}\right)_{F,g} \right]^{0.5}. \quad (20)$$

A list of correlations for C [48–53] assessed in this study are listed in Table 3. Some empirical correlations slightly deviate from the general procedure noted in Eqs. (12)-(20); these are listed in Table 4.

4.3. Prediction Performance of Pressure Drop Models for Saturated Flow Boiling

To evaluate the prediction performance of Δp models for the saturated flow boiling regime, only the experiments with saturated flow boiling all along the channel length are considered, which is a total of N = 1099 datapoints with both $0 \le x_{e,in} \le 1$ and $0 \le x_{e,out} \le 1$. The assessment results of several HEM and SFM-based seminal relations are reported in Table 5 in terms of MAE for the entire saturated flow boiling subset of the μg_e database. To verify if each relation's prediction accuracy is skewed towards certain operating conditions, MAEs are also reported for smaller subsets of data, demarcated based on the heating configuration (single *vs*. double), $x_{e,in}$ (low *vs*. high quality with a threshold of 0.2), and G (low *vs*. high velocity with a threshold of 1200 kg/m^{2}s).

4.3.1. Prediction Performance of the HEM-based Mixture Viscosity Models

Overall, HEM-based mixture viscosity relations have MAEs of 26-45%. HEM is more applicable for flow scenarios where the liquid and vapor phases are well mixed, bubbly flows for example. In general, the HEM predicts double-sided heating data slightly better than single-sided because of more uniform phase change across the channel cross-section resulting in better phase mixing. Moreover, the relations were originally developed for either adiabatic or uniform heat addition from all walls. Low qualities are predicted well by McAdams *et al.* [38], Dukler *et al.* [42,43], Beattie and Whalley [44], and Lin *et al.* [45] while high qualities by Akers *et al.* [39], Cicchitti *et al.* [40], and Owens [41]. This is because the latter set of relations yield higher μ_{tp} at high x_e compared to the others (which can be seen by inspecting the trend of μ_{tp} versus x_e predicted by each model), and this might be representative of the actual μ_{tp} in μg_e at these qualities. In fact, all relations predict low-quality data with 36-39% MAE. Δp for low G is significantly predicted well by all HEM μ_{tp} models compared to high G.

Table 2
Summary of HEM-based two-phase mixture viscosity models.

Author(s) (Year)	Equation(s)
McAdams *et al.* (1942) [38]	$\frac{1}{\mu_{tp}} = \frac{x_e}{\mu_g} + \frac{1 - x_e}{\mu_f}$
Akers *et al.* (1959) [39]	$\mu_{tp} = \mu_f \Big/ \left[(1 - x_e) + x_e \left(\frac{v_g}{v_f}\right)^{0.5}\right]$
Cicchitti *et al.* (1960) [40]	$\mu_{tp} = x_e \mu_g + (1 - x_e)\mu_f$
Owens (1961) [41]	$\mu_{tp} = \mu_f$
Dukler *et al.* (1964) [42,43]	$\mu_{tp} = \frac{x_e v_g \mu_g + (1 - x_e) v_f \mu_f}{x_e v_g + (1 - x_e) v_f}$
Beattie & Whalley (1982) [44]	$\mu_{tp} = \omega \mu_g + (1 - \omega)(1 + 2.5\omega)\mu_f$; $\omega = \frac{x_e v_g}{v_f + x_e v_{fg}}$
Lin *et al.* (1991) [45]	$\mu_{tp} = \frac{\mu_f \mu_g}{\mu_g + x_e^{1.4}\left(\mu_f - \mu_g\right)}$

The six best performing μ_{tp} models are further examined in the parity plots in Fig. 9, plotted as Δp_{pred} versus Δp_{exp}, and datapoints segregated based on $x_{e,in}$. The best HEM predictions are provided using Owens' [41] relation, which is simply equal to the liquid viscosity at all qualities, with a 26.7% MAE and 90% of datapoints predicted within ±50%. All six models show an even spread over the entire Δp range both over and underestimating experimental values, with higher MAEs by some models mostly a result of more datapoints underpredicted over the entire range (while very few datapoints lie above the +30% line). Comparing low and high $x_{e,in}$, the $x_{e,in} \ge 0.2$ data have less spread and are mostly underpredicted over the entire range. Some $x_{e,in} < 0.2$ data are scattered in lower right of the figures, and these are expected to be datapoints with significant measurement errors.

4.3.2. Prediction Performance of the SFM-based Correlations

The SFM-based relations have a broad range of predictive accuracies with MAEs of 17.1-231.8%. This is mainly because of the greater empiricism in these relations, meaning that the empirical relations and constants are more reliant on the database used to develop them, making them applicable only over those specific conditions. The best overall predictions are provided by the original relations of Lockhart and Martinelli [48] with an overall MAE of just 17.1%. This is because these values were developed over a range of fluids in the early years for macro-channels and a wide range of pressures, which are apt for the present database values, albeit for adiabatic conditions. On the other hand, the worst predictions are provided by Yan and Lin's [58] correlation because it was developed based on just one set of experiments of R134a flow boiling in a 2 mm diameter tube over a very narrow range of operating conditions. Looking closely, the correlations which were developed based on fewer datapoints (representative of only one experiment or a few, especially in micro-channels) [50–52,55,56,58–60] generally yield much worse predictions compared to the ones developed using large, consolidated databases [48,49,53,61–64]. This demonstrates the need to carefully review the applicability criteria of each empirical correlation before use. Lee and Mudawar [52] provided a correlation each for *vt* and *vv* regimes, however the liquid is turbulent in the present study, so predictions could not be made.

There is no consistent trend in the predictive accuracies for single *vs*. double-sided heating with each correlation predicting one heating configuration marginally better than the other. The six best-performing correlations predict the single-sided data marginally better than double-sided and the $x_{e,in} \ge 0.2$ data better than the $x_{e,in} < 0.2$ data because the

Table 3
Summary of SFM-based empirical relations for C. To be used along with the general relations in Eqs. (12)-(20).

Author(s) (Year)	Equation(s)	Remarks
Lockhart & Martinelli (1949) [48]	$C=\begin{cases}20, & \mathrm{Re}_f\ge 2000, \mathrm{Re}_g\ge 2000 (tt)\\ 10, & \mathrm{Re}_f\ge 2000, \mathrm{Re}_g< 2000 (tv)\\ 12, & \mathrm{Re}_f< 2000, \mathrm{Re}_g\ge 2000 (vt)\\ 5, & \mathrm{Re}_f< 2000, \mathrm{Re}_g< 2000 (vv)\end{cases}$	Adiabatic: Water, oil, benzene, kerosene D_h = 1.49 – 25.83 mm p = 110 – 360 kPa
Mishima & Hibiki (1996) [49]	$C=\begin{cases}21\left(1-\exp\left(-0.319\times 10^3 D_h\right)\right), & \text{rectangular channel}\\ 21\left(1-\exp\left(-0.333\times 10^3 D\right)\right), & \text{circular channel}\end{cases}$	Adiabatic: Air-water, ammonia-vapor, R113-N2 D_h = 0.7 – 25.37 mm
Lee & Lee (2001) [50]	$C=\begin{cases}0.048\mathrm{Re}_{fo}^{0.451}, & \mathrm{Re}_f\ge 2000, \mathrm{Re}_g\ge 2000 (tt)\\ 3.627\mathrm{Re}_{fo}^{0.174}, & \mathrm{Re}_f\ge 2000, \mathrm{Re}_g< 2000 (tv)\\ 6.185\times 10^{-2}\mathrm{Re}_{fo}^{0.726}, & \mathrm{Re}_f< 2000, \mathrm{Re}_g\ge 2000 (vt)\\ 6.833\times 10^{-8}\lambda^{-1.317}\psi^{0.719}\mathrm{Re}_{fo}^{0.557}, & \mathrm{Re}_f< 2000, \mathrm{Re}_g< 2000 (vv)\end{cases}$ $\psi=\frac{\mu_f j_f}{\sigma},\ \lambda=\frac{\mu_f^2}{\rho_f\sigma D_h}$	Adiabatic: Air-water D_h = 0.78 – 6.67 mm H = 0.4 – 4 mm W = 20 mm j_f = 0.03 – 2.39 m/s j_g = 0.05 – 18.7 m/s X = 0.303 – 79.4 Re_{fo} = 175 - 17700
Qu & Mudawar (2003) [51]	$C=21\left[1-\exp\left(-0.319\times 10^3 D_h\right)\right](0.00418G+0.0613)$	Boiling: Water D_h = 348.9 μm H = 713 μm; W = 231 μm
Lee & Mudawar (2005) [52]	$C=\begin{cases}1.45\mathrm{Re}_{fo}^{0.25}We_{fo}^{0.23}, & \mathrm{Re}_f< 2000, \mathrm{Re}_g\ge 2000 (vt)\\ 2.16\mathrm{Re}_{fo}^{0.047}We_{fo}^{0.60}, & \mathrm{Re}_f< 2000, \mathrm{Re}_g< 2000 (vv)\end{cases}$	Boiling: R134a H = 713 μm W = 231 μm
Kim & Mudawar (2013) [53]	$\mathrm{Re}_{fo}=\frac{GD_h}{\mu_f}$ $C_{non-boiling}=$ $\begin{cases}0.39\mathrm{Re}_{fo}^{0.03}Su_{go}^{0.10}\left(\rho_f/\rho_g\right)^{0.35}, & \mathrm{Re}_f\ge 2000, \mathrm{Re}_g\ge 2000 (tt)\\ 8.7\times 10^{-4}\mathrm{Re}_{fo}^{0.17}Su_{go}^{0.50}\left(\rho_f/\rho_g\right)^{0.14}, & \mathrm{Re}_f\ge 2000, \mathrm{Re}_g< 2000 (tv)\\ 0.0015\mathrm{Re}_{fo}^{0.59}Su_{go}^{0.19}\left(\rho_f/\rho_g\right)^{0.36}, & \mathrm{Re}_f< 2000, \mathrm{Re}_g\ge 2000 (vt)\\ 3.5\times 10^{-5}\mathrm{Re}_{fo}^{0.44}Su_{go}^{0.50}\left(\rho_f/\rho_g\right)^{0.48}, & \mathrm{Re}_f< 2000, \mathrm{Re}_g< 2000 (vv)\end{cases}$ $C=\begin{cases}C_{non-boiling}\left[1+60We_{fo}^{0.32}\left(Bo\frac{P_h}{P_f}\right)^{0.78}\right], & \mathrm{Re}_f\ge 2000\\ C_{non-boiling}\left[1+530We_{fo}^{0.52}\left(Bo\frac{P_h}{P_f}\right)^{1.09}\right], & \mathrm{Re}_f< 2000\end{cases}$	Boiling: Water, R12, R134a, CO_2, R410A, R22, R245fa, FC72, ammonia D_h = 0.349 – 5.35 mm Re_{fo} =156 – 28010 p_r = 0.005 – 0.78

corresponding observed flow regimes have their phases well separated, making the SFM well applicable. For example, the Lockhart and Martinelli relation predicts the higher $x_{e,in}$ data with a low 14.1% MAE and the lower $x_{e,in}$ data with a relatively high 22.5% MAE. Similar to the HEM, the SFM predicts the low G data significantly better, perhaps with a smaller difference between the two G sets, when compared to the HEM.

Table 5 also shows identical prediction results by HEM-based Beattie and Whalley [44] and SFM-based Li and Wu (both [62] and [63]). This is due to the suggestion by Li and Wu to use the Beattie and Whalley μ_{tp} model for conditions with $Bd > 11$ [62] or $BdRe_f^{0.5} > 200$ [63], which is satisfied by the entire present database.

The six best performing SFM relations are further examined in the parity plots in Fig. 10, plotted as Δp_{pred} versus Δp_{exp}, and datapoints segregated based on $x_{e,in}$. Lockhart and Martinelli's relation yields both over and underpredictions of data spread almost symmetrically over the entire range about the 45° 0%-error line. Following Lockhart and Martinelli, Kim and Mudawar's [53] correlation yields the second-best accuracy with a 23.2% MAE and 91.3% of datapoints predicted within ±50%. This is because the correlation was developed based on a large database that spanned multiple geometries, several fluids, and broad ranges of operating conditions, which encompasses the present study's parameters. Also, this correlation incorporates the ratio of heated to friction perimeters, P_h/P_f, while most others do not. Predicting Δp without considering this ratio significantly worsens the MAE to 92.1%, highlighting the importance of this dimensionless group. Both Lockhart and Martinelli [48] and Mishima and Hibiki's [49] relations yield the narrowest scatter of predictions with > 97% of datapoints predicted within ±50%, while the other relations have larger scatter. This scatter consists of mostly underpredictions for the low $x_{e,in}$ data, while the high $x_{e,in}$ data has both over and underpredictions.

4.4. Pressure Drop for Subcooled Flow Boiling

Subcooled flow boiling is the boiling regime where the local bulk fluid temperature is lower than the saturation temperature at local pressure, *i.e.*, where thermodynamic equilibrium quality, $x_e < 0$, but void fraction, $\alpha > 0$. Pressure drop for subcooled flow boiling, Δp_{sc}, is typically smaller than that for saturated flow boiling, Δp_{sb}, due to the corresponding two-phase physics. Also, in most applications, subcooled flow boiling covers a short distance compared to saturated flow boiling and the associated pressure drop is insignificant, so Δp_{sc} is approximated as the single-phase pressure drop. This is the reason why most Δp studies in literature are focused on saturated flow boiling, and very few are available for subcooled boiling. Δp_{sc} is typically determined using empirical correlations, which take the form,

$$\frac{\Delta p_{sc}}{\Delta p_{sp,f}}=\phi_{sc}^2, \tag{21}$$

where $\Delta p_{sp,f}$ is single-phase liquid adiabatic pressure drop given as

$$\Delta p_{sp,f}=\frac{2f_{sp,f}G^2L}{\rho_f D_h} \tag{22}$$

and ϕ_{sc}^2 is subcooled pressure drop multiplier. Single-phase liquid friction factor is expressed for rectangular channels as

Table 4
Summary of seminal correlations for frictional pressure gradient following the SFM approach.

Author(s)	Equation(s)	Remarks
Müller-Steinhagen & Heck (1986) [54]	$\left(\frac{dp}{dz}\right)_F = \left\{\left(\frac{dp}{dz}\right)_{fo} + 2\left[\left(\frac{dp}{dz}\right)_{go} - \left(\frac{dp}{dz}\right)_{fo}\right]x_e\right\}(1-x_e)^{1/3} + \left(\frac{dp}{dz}\right)_{go} x_e^3$	Adiabatic: Air-water, air-oil, argon, argon-ethanol, argon-water, steam-water, hydrocarbons, neon, nitrogen, R11, R12, R12 $D = 4 - 392$ mm
Jung & Radermacher (1989) [55]	$\left(\frac{dp}{dz}\right)_F = \left(\frac{dp}{dz}\right)_{fo}\phi_{fo}^2;\ \phi_{fo}^2 = 12.82X_{tt}^{-1.47}(1-x_e)^{1.8};\ X_{tt} = \left(\frac{\mu_f}{\mu_g}\right)^{0.1}\left(\frac{1-x_e}{x_e}\right)^{0.9}\left(\frac{\rho_g}{\rho_f}\right)^{0.5}$	Annular flow boiling: Pure and mixed refrigerants $D = 9.1$ mm
Yang & Webb (1996) [56]	$\left(\frac{dp}{dz}\right)_F = -0.87\,Re_e^{0.12} f_{fo}\frac{G_{eq}^2 v_f}{D_h};\ Re_{eq} = \frac{G_{eq}D_h}{\mu_f};\ G_{eq} = G\left[(1-x_e) + x_e\left(\frac{\rho_f}{\rho_g}\right)^{0.5}\right]$	Adiabatic: R12 $D = 1.56 - 2.64$ mm $Re_{fo} > 2500$
Wang *et al.* (1997) [57]	For $G \geq 200$ kg/m^{2}s, $\left(\frac{dp}{dz}\right)_F = \left(\frac{dp}{dz}\right)_g \phi_g^2;\ \phi_g^2 = 1 + 9.4X^{0.62} + 0.564X^{2.45}$ For $G < 200$ kg/m^{2}s, $\left(\frac{dp}{dz}\right)_F = \left(\frac{dp}{dz}\right)_f \phi_f^2;\ \phi_f^2 = 1 + \frac{C}{X} + \frac{1}{X^2};\ C = 4.566 \times 10^{-6} X^{0.128} Re_{fo}^{0.938}\left(\frac{v_f}{v_g}\right)^{2.15}\left(\frac{\mu_f}{\mu_g}\right)^{5.1}$	Adiabatic: R22, R134a, R407C $D = 6.5$ mm
Yan & Lin (1998) [58]	$\left(\frac{dp}{dz}\right)_F = -0.22\,Re_e^{-0.1}\frac{G^2}{D_h}\left[v_f + x_e v_{fg}\right]$	Boiling: R134a $D = 2.0$ mm
Tran *et al.* (2000) [59]	$\left(\frac{dp}{dz}\right)_F = \left(\frac{dp}{dz}\right)_{fo}\phi_{fo}^2;\ \phi_{fo}^2 = 1 + \left[4.3\frac{(dp/dz)_{go}}{(dp/dz)_{fo}} - 1\right]\left[N_{conf} x_e^{0.875}(1-x_e)^{0.875} + x_e^{1.75}\right]$	Boiling: R134a, R12, R113 $D_h = 2.40 - 2.92$ mm $p = 138 - 856$ kPa, $p_r = 0.04 - 0.23$
Yu *et al.* (2002) [60]	$\left(\frac{dp}{dz}\right)_F = \left(\frac{dp}{dz}\right)_f \phi_f^2;\ \phi_f^2 = \left[18.65\left(\frac{v_f}{v_g}\right)^{0.5}\left(\frac{1-x_e}{x_e}\right)\frac{\mathrm{Re}_g^{0.1}}{\mathrm{Re}_f^{0.5}}\right]^{-1.9}$	Boiling: Water $D = 2.98$ mm
Sun & Mishima (2009) [61]	$\left(\frac{dp}{dz}\right)_F = \left(\frac{dp}{dz}\right)_f \phi_f^2$ For $Re_f < 2000$ and $Re_g < 2000$, $\phi_f^2 = 1 + \frac{C}{X} + \frac{1}{X^2};\ C = 26\left(1 + \frac{\mathrm{Re}_f}{1000}\right)\left\{1 - \exp\left(\frac{-0.153}{0.27\,N_{conf} + 0.8}\right)\right\}$ For $Re_f \geq 2000$ or $Re_g \geq 2000$, $\phi_f^2 = 1 + \frac{C}{X^{1.19}} + \frac{1}{X^2};\ C = 1.79\left(\frac{Re_g}{Re_f}\right)^{0.4}\left(\frac{1-x_e}{x_e}\right)^{0.5}$	Adiabatic: Air-water, R134a, R22, R236ea, R245fa, R407C, R410a Boiling: Water, CO_2, R123, R134a, R22, R402a, R404a, R407C, R410A, R502, R507 Condensing: R134a $D_h = 0.506 - 12$ mm $Re_f = 10 - 37000$ $Re_g = 3 - 4 \times 10^5$
Li & Wu (2010) [62]	$\left(\frac{dp}{dz}\right)_F = \left(\frac{dp}{dz}\right)_f \phi_f^2;\ \phi_f^2 = 1 + \frac{C}{X} + \frac{1}{X^2}$ For $Bd \leq 1.5$, $C = 11.9\,Bd^{0.45}$ For $1.5 < Bd \leq 11$, $C = 109.4\left(Bd\,Re_f^{0.5}\right)^{-0.56}$ For $Bd > 11$, use HEM with Beattie & Whalley's [44] μ_{tp} relation	Adiabatic: R134a, R245fa, R236ea, R410a, R22, R404a, R12, R422d, R32, ammonia, propane, N2 $D_h = 0.148 - 3.25$ mm $G = 140 - 2000$ kg/m^{2}s
Li & Wu (2011) [63]	For $Bd < 0.1$, $\left(\frac{dp}{dz}\right)_F = \left(\frac{dp}{dz}\right)_f \phi_f^2;\ \phi_f^2 = 1 + \frac{C}{X} + \frac{1}{X^2};\ C = 5.60Bd^{0.28}$ For $Bd \geq 0.1$ and $Bd\mathrm{Re}_f^{0.5} \leq 200$, $\left(\frac{dp}{dz}\right)_F = \left(\frac{dp}{dz}\right)_{fo}\phi_{fo}^2;\ \phi_{fo}^2 = (1-x_e)^2 + 2.87x_e^2 p_r^{-1} + 1.54Bd^{0.19}\left(\frac{\rho_f - \rho_g}{\rho_{tp}}\right)^{0.81}$ For $Bd\mathrm{Re}_f^{0.5} > 200$, use HEM with Beattie & Whalley's [44] μ_{tp} relation	Adiabatic: R134a, R245fa, R236ea, R410a, R22, R404a, R12, R422d, R32, ammonia, propane, N2 $D_h = 0.148 - 3.25$ mm $G = 140 - 2000$ kg/m^{2}s
Ma *et al.* (2024) [64]	$\left(\frac{dp}{dz}\right)_F = \left(\frac{dp}{dz}\right)_f \phi_f^2;\ \phi_f^2 = \left[1 + 2690\left(\frac{Bd^{0.97}}{X_{tt}^{0.43} p_r^{0.95}}\right)\right]\mathrm{Re}_f^{1.03} We_{fo}^{0.53}$ $X_{tt} = \left(\frac{1-x_e}{x_e}\right)^{0.9}\left(\frac{\rho_g}{\rho_f}\right)^{0.5}\left(\frac{\mu_f}{\mu_g}\right)^{0.1}$	Boiling: Water, R134a, CO_2, R236fa, R245fa, HFE 7100, R1234yf, R1233zd(E), R1234ze(E), acetone, R600a $D_h = 0.1 - 2.6$ mm $G = 50 - 3000$ kg/m^{2}s $p = 101 - 3970$ kPa

$$f_{sp,f} = \begin{cases} 24\left(1 - 1.3553\beta + 1.9467\beta^2 - 1.7012\beta^3 \\ +0.9564\beta^4 - 0.2537\beta^5\right) Re_{sp,f}^{-1}, & Re_{sp,f} < 2000 \\ 0.079 Re_{sp,f}^{-0.25}, & 2000 \le Re_{sp,f} < 20000' \\ 0.046 Re_{sp,f}^{-0.2}, & Re_{sp,f} \ge 20000 \end{cases} \quad (23)$$

where single-phase liquid Reynolds number is defined as

$$\mathrm{Re}_{sp,f} = \frac{GD_h}{\mu_f}. \quad (24)$$

ϕ_{sc}^2 is empirically derived and takes various functional forms, dependent on thermophysical properties, geometrical parameters, and operating conditions. When either heat flux is zero or bubble nucleation is absent, $\Delta p_{sc} = \Delta p_{sp,f}$ and $\phi_{sc}^2 = 1$. As heat flux is increased, the fluid temperature rises, small bubbles nucleate at the channel walls, and flow viscosity reduces, resulting in an initial small decrease in Δp and $\phi_{sc}^2 < 1$. A short distance downstream within the subcooled boiling regime or at even higher heat fluxes, significant vapor production results in flow acceleration and larger pressure drop with $\phi_{sc}^2 > 1$.

A summary of seminal correlations for ϕ_{sc}^2 [36,65–71] is presented in Table 6 along with remarks on the working fluid and geometrical and operating parameters based on which they were developed. Overall, $\Delta p_{sc} > \Delta p_{sp,f}$, so $\phi_{sc}^2 > 1$, which is evident in the functional form of (1 + positive parameters) in Tarasova *et al.* [66], Hahne *et al.* [67], Baburajan *et al.* [69], Yan *et al.* [70], and Ramesh and Gedupudi [71].

The ϕ_{sc}^2 expressions are typically dependent on two lengths: (i) subcooled boiling length, L_{sc}, defined as the distance from the ONB location to the location where subcooled boiling ends (this is the channel exit if the fluid exits in subcooled state or the physical location where $x_e = 0$ if the channel is long enough for the fluid to attain saturation), and (ii) boiling length to attain saturation, L_{sat}, defined as the distance from the ONB location to the location where the fluid would attain saturation, $x_e = 0$. The latter is determined as a result of energy balance within the channel,

$$L_{sat} = \frac{GA_c}{q'' P_h} c_{p,f}\left(T_{sat} - T_f\right), \quad (25)$$

where the temperature difference is estimated at the channel inlet because of the negligible influence of upstream $\Delta p_{sp,f}$ on the channel's Δp_{tot}.

4.5. Prediction Performance of Pressure Drop Correlations for Subcooled Flow Boiling

To evaluate the prediction performance of Δp correlations for the subcooled flow boiling regime, only the experiments with subcooled flow boiling all along the channel length are considered, which is a total of $N = 1065$ datapoints with $x_{e,in} < 0$, $x_{e,out} < 0$, and ONB commencing near the channel inlet. Assessment results in terms of MAE are reported

Table 5
Mean absolute errors (%) of seminal models/correlations for pressure drop of saturated flow boiling.

Model/ Correlation	Total (1099 data points)	Single-sided (446 data points)	Double-sided (653 data points)	$x_{e,in} < 0.2$ (393 data points)	$x_{e,in} \ge 0.2$ (706 data points)	$G < 1200$ kg/m^{2}s (1034 data points)	$G \ge 1200$ kg/m^{2}s (65 data points)
HEM based							
McAdams *et al.* (1942) [38]	42.1	44.1	40.8	37.3	44.8	40.3	71.3
Akers *et al.* (1959) [39]	34.8	36.0	34.0	35.6	34.3	32.8	66.1
Cicchitti *et al.* (1960) [40]	27.7	27.4	27.9	36.0	23.2	25.7	60.1
Owens (1961) [41]	26.7	26.2	27.1	36.3	21.4	24.7	58.5
Dukler *et al.* (1964) [42, 43]	44.4	46.4	43.0	38.7	47.6	42.4	75.5
Beattie & Whalley (1982) [44]	40.9	43.0	39.5	36.2	43.6	39.2	68.9
Lin *et al.* (1991) [45]	40.2	42.3	38.8	36.1	42.5	38.5	67.8
SFM based							
Lockhart & Martinelli (1949) [48]	17.1	16.2	17.7	22.5	14.1	16.7	22.6
Müller-Steinhagen & Heck (1986) [54]	68.8	70.3	67.8	68.9	68.7	67.4	90.8
Jung & Radermacher (1989) [55]	62.0	62.5	61.7	65.4	60.2	60.3	89.7
Mishima & Hibiki (1996) [49]	25.1	23.6	26.2	26.8	24.2	24.2	40.2
Yang & Webb (1996) [56]	43.0	40.8	44.4	51.9	38.0	41.0	73.9
Wang *et al.* (1997) [57]	26.7	23.1	29.2	35.3	22.0	24.7	59.8
Yan & Lin (1998) [58]	231.8	263.3	210.2	178.8	261.3	234.0	196.6
Tran *et al.* (2000) [59]	49.0	49.6	48.5	94.7	23.5	41.2	172.5
Lee & Lee (2001) [50]	52.9	53.3	52.7	61.5	48.2	51.3	78.5
Yu *et al.* (2002) [60]	61.8	62.7	61.1	64.2	60.4	60.5	82.3
Qu & Mudawar (2003) [51]	69.6	68.6	70.3	113.6	45.1	54.8	304.8
Sun & Mishima (2009) [61]	37.4	35.6	38.7	40.5	35.7	35.9	61.5
Li & Wu (2010) [62]	40.9	43.0	39.5	36.2	43.6	39.2	68.9
Li & Wu (2011) [63]	40.9	43.0	39.5	36.2	43.6	39.2	68.9
Kim & Mudawar (2013) [53]	23.2	22.0	24.1	23.8	22.9	23.1	25.2
Ma *et al.* (2024) [64]	39.4	38.8	39.8	40.8	38.6	37.2	74.1

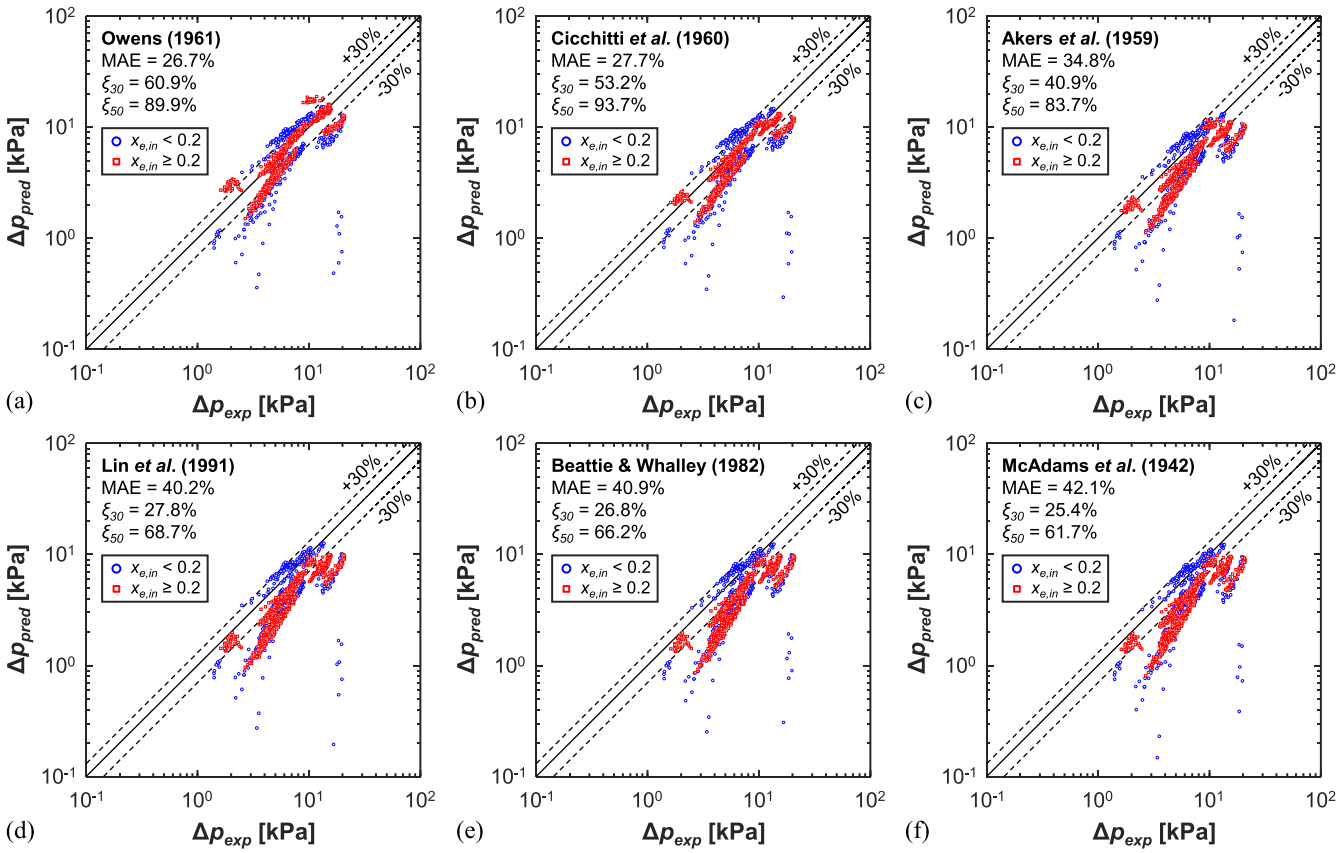

Fig. 9. Parity plots assessing the predictive performance of HEM-based mixture viscosity models for saturated flow boiling pressure drop: (a) Owens (1961), (b) Cicchitti et al. (1960), (c) Akers et al. (1959), (d) Lin et al. (1991), (e) Beattie & Whalley (1982), and (f) McAdams et al. (1942).

in Table 7 for the entire subcooled flow boiling subset of the μg_e database. MAEs are also reported for smaller subsets of data, demarcated based on the heating configuration (single *vs.* double), $\Delta T_{sub,in}$ (highly subcooled inlet for $\Delta T_{sub,in} > 10°C$ *vs.* near-saturated inlet for $\Delta T_{sub,in} \leq 10°C$ [22,29]), and G (low *vs.* high velocity with a threshold of 1200 kg/m^{2}s). Note that the predictions were skipped for some datapoints in case $Ja^* < 10^{-4}$ (so some correlations yield $\Delta p \rightarrow \infty$ since Ja^* is often raised to a negative exponent), $L_{sat} < 0$ (so flow becomes locally saturated, making some correlations yield complex numbers for Δp), or local pressure goes out of the range for which thermophysical properties are available (so computations could not proceed further). Inclusion of lengths in the ϕ_{sc}^2 correlation, be it L, L_{sc}, or L_{sat}, means the Δp_{pred} would be different based on whether ϕ_{sc}^2 is evaluated for the entire channel as a whole based on inlet properties or is re-evaluated for each channel segment based on local properties; the former is adopted in this study because of how the original correlations were developed.

The best predictions are provided by the correlation by Hahne *et al.* [67] with empirical constant $C = 80$, evidenced by a 34.1% MAE. On the other hand, the worst (and completely non-physical) predictions are provided by the correlation by Tarasova *et al.* [66] with a 182.6% MAE, so this is excluded from further discussion. Heating configuration has a mixed accuracy response with Owens and Schrock [65] predicting with virtually no difference, Hahne *et al.* [67] predicting single-sided with significantly better accuracy while the others [36,68–71] predict double-sided significantly better. The correlations yield mixed prediction accuracies when considering highly subcooled *vs.* near-saturated inlets and low *vs.* high G.

The six best performing ϕ_{sc}^2 correlations are further examined in the parity plots in Fig. 11, plotted as Δp_{pred} versus Δp_{exp}, and datapoints segregated based on $\Delta T_{sub,in}$. The correlations by Owens and Schrock [65], Hahne *et al.* [67] with $C = 80$, and Tong *et al.* [68] with $C = 1.35$ generally underpredict the data across the entire Δp range. On the other hand, Hahne *et al.* with $C = 500$ and Baburajan *et al.* [69] generally overpredicts the data across the entire Δp range. Hahne *et al.* developed their correlation for different classes of fluids and tuned their leading empirical constant to $C = 80$ for water (underpredictions for nPFH) and 500 for refrigerants (overpredictions for nPFH). nPFH has thermophysical properties somewhat intermediary between these 2 fluids, meaning better prediction would be achieved with an appropriately tuned C between 80 and 500. Similarly, Tong *et al.* has two distinct C values, 1.35 for $L/D = 25$ and 0.4 for $L/D = 50$, while $L/D = 34.4$ for the present channel. Nevertheless, the correlation is developed for water alone and is only dependent on L_{sc}/L_{sat}, so the prediction would remain poor even if C is tuned. Figs. 11(d) and (e) show both Tong et al. and Kim and Mudawar to have large spreads of predictions for the same Δp_{exp}, meaning some important nPFH macro-channel boiling physics is not captured in their correlations (the former was developed only for water with very high G, while the latter for small micro-channels, so not applicable). The reported correlation of Ma *et al.* [64] contains the Lockhart-Martinelli parameter, which is not directly applicable for subcooled boiling, so predictions are not made.

Overall, several seminal models/correlations for saturated flow boiling are more capable of predicting Δp for the present μg_e database compared to the seminal correlations for subcooled flow boiling. This is because the latter has received less attention in the literature because of typically low Δp_{sc} compared to Δp_{sb}, and very few correlations exist, none of which are directly applicable to the conditions in the present study. Note that for the present data, Δp_{sc} and Δp_{sb} are of the same order of magnitude.

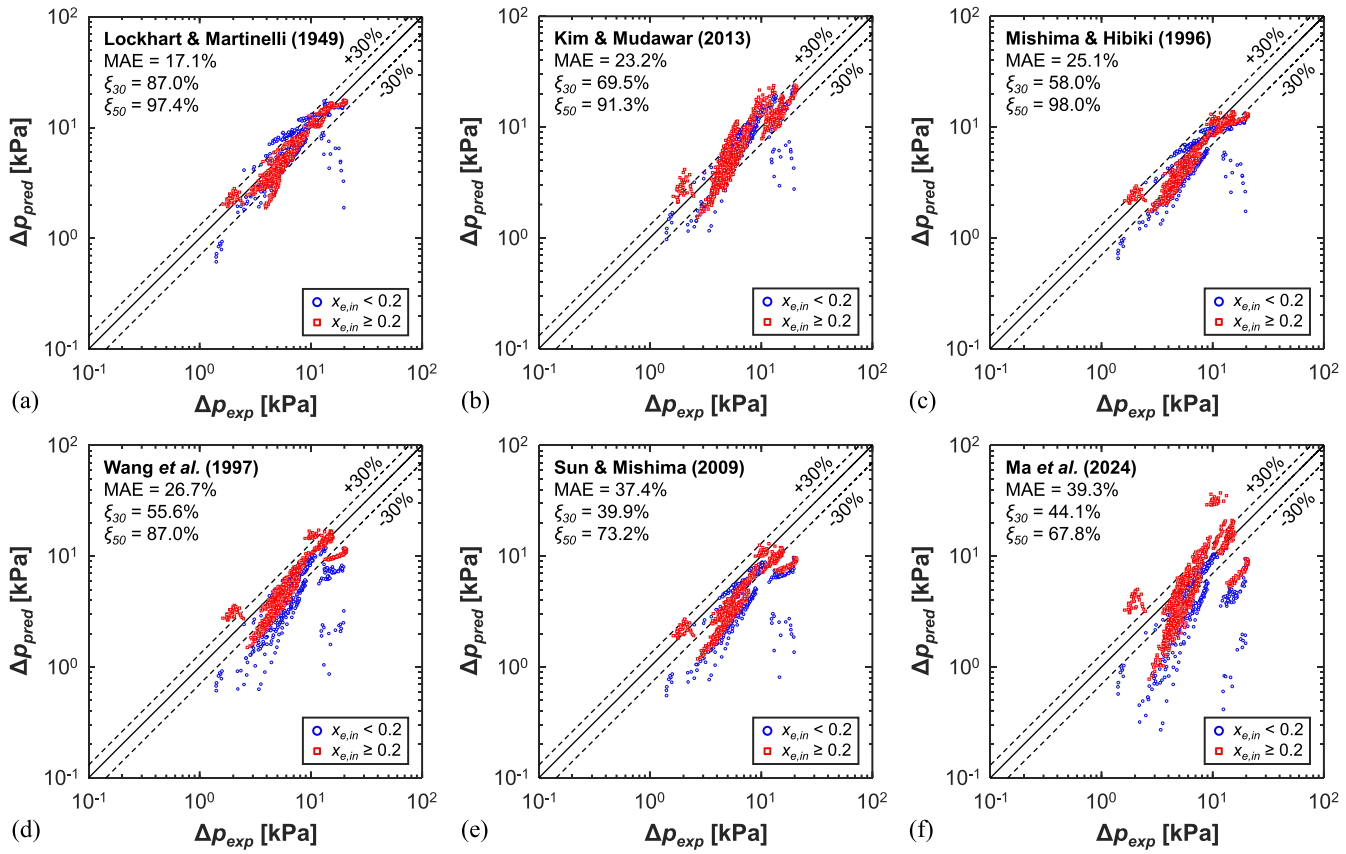

Fig. 10. Parity plots assessing the predictive performance of SFM-based semi-empirical correlations for saturated flow boiling pressure drop: (a) Lockhart & Martinelli (1949), (b) Kim & Mudawar (2013), (c) Mishima & Hibiki (1996), (d) Wang *et al.* (1997), (e) Sun & Mishima (2009), and (f) Ma *et al.* (2024).

5. Application of Artificial Neural Networks (ANNs) to Predict Flow Boiling Pressure Drop in Microgravity

5.1. Overview of ANNs

Artificial neural networks (ANNs) are black box models capable of tackling prediction, pattern recognition, optimization, and classification problems [72]. Their main advantages stem from their (i) nonlinearity capturing complex trends in data, (ii) noise-insensitivity providing accurate predictions even in the presence of measurement uncertainties, (iii) parallelism resulting in fast processing and fault tolerance, (iv) learning and adaptability to accommodate a changing environment, and (v) generalization to new data [73]. This has enticed numerous researchers to develop ANNs capable of predicting various aspects of two-phase flows. Some examples include Guanghui *et al.* [74] for CHF in natural circulation or low pressure pumped flow loops, Qiu *et al.* [75] [76] for heat transfer of saturated flow boiling, Cho *et al.* [77] for heat transfer of a free-falling condensing film, and the present authors [31] for heat transfer and CHF of flow boiling as part of FBCE. The present study utilizes the same methodology to develop an ANN for predicting pressure drop in μg_e. A brief description of the algorithms, training parameters, and network development process used is provided here; further details can be found in [31].

Fig. 12 depicts the typical structure of a fully connected feed-forward ANN, which is comprised of a densely interconnected web of neurons. Sizes of the first and last layer, *aka* input and output layer, are determined by the desired number of input and output parameters, respectively. The intermediate layers are called *hidden layers*. A network contains one or more hidden layers, each containing any number of neurons. In a fully connected neural network, each neuron in a given layer is connected to each neuron in the previous and following layers, as shown in Fig. 12. In feed-forward networks, information propagates from the input layer towards the output layer, such that the outputs of the neurons from one layer serve as the inputs for the neurons in the following layer. Also shown in Fig. 12 is the operation of a neuron, which follows the original modeling of a neuron by McCulloch and Pitts [78] as a switch. This is accomplished by the inputs of each neuron x_i, being multiplied by an associated weight w_i, and added to a bias b. The weighted sum of the inputs and the bias, v, is then passed through a nonlinear activation function $f(v)$, to produce an output y. The present study employs the rectified linear unit (ReLu) function as the activation function, which is calculated as

$$f(v) = \begin{cases} v, & v \geq 0 \\ 0, & v < 0 \end{cases}. \tag{26}$$

The main advantages of the ReLu activation function are its simplicity, mitigation of the vanishing gradient problem, and efficiency during training with gradient descent training algorithms [79].

During the training process, the ANN *learns* the data by tuning the weights and bias to minimize the loss function. Half of the Mean Squared Error (MSE) of the outputs is typically used as the loss function during regression problems. For a single output, it is calculated as

$$E = \frac{1}{2}\sum_{i=1}^{n}(y_i - t_i)^2, \tag{27}$$

where E is the loss, y_i and t_i are the predicted and target output of an observation i, respectively, and n is the total number of observations in each iteration. The *back propagation algorithm* [80] is a commonly used gradient descent technique for training multi-layer, feed-forward neural networks. It updates the weights and biases to minimize the loss with the gradient of the loss function, which is explicitly determined at the output layer and is propagated backward to the input layer, and the selected

Table 6
Summary of seminal correlations for pressure drop of subcooled flow boiling.

Author(s)	Equation(s)	Remarks
Owens & Schrock (1960) [65]	$\phi_{sc}^2 = 0.97 + 0.028\exp\left(6.13\frac{L_{sc}}{L_{sat}}\right)$	Water D = 3 – 4.63 mm G = 1143 – 5322 kg/m^{2}s p = 340 – 2760 kPa q'' = 67.5 – 400.6 W/cm^2
Tarasova *et al.* (1966) [66]	$\phi_{sc}^2 = 1 + Bo^{0.7}\left(\frac{\rho_f}{\rho_g}\right)^{0.78}\frac{20(L_{sc}/L_{sat})}{1.135-(L_{sc}/L_{sat})}$	Water D = 2.89 – 8.31 mm G = 1400 – 3000 kg/m^{2}s p = 980 – 19600 kPa q'' = 58 – 175 W/cm^2
Hahne *et al.* (1993) [67]	$\phi_{sc}^2 = 1 + C.Bo^{1.6}Ja*^{-1.2}\left(\frac{\rho_f}{\rho_g}\right)\left(\frac{P_h}{P_f}\right)$ C = 80 for water C = 500 for R12 and R134a	Water, R12, R134a D_h = 9.53 – 20 mm G = 750 – 3200 kg/m^{2}s p = 300 – 2000 kPa q'' = 0.52 – 96 W/cm^2
Tong *et al.* (1997) [68]	$\phi_{sc}^2 = \left(\frac{L_{sc}}{L_{sat}}\right)^{1.3}\exp\left(\frac{L_{sc}}{L_{sat}}+C\right)$ C = 1.35 for L/D = 25 C = 0.4 for L/D = 50	Water D = 1.05 – 2.44 mm G = 25000 – 45000 kg/m^{2}s p = 400 – 1600 kPa q'' < 8000 W/cm^2
Kim & Mudawar (2012) [36]	$\phi_{sc}^2 = 20.73Ja*^{-0.98}\beta^{0.42}\left(\frac{L}{D_h}\right)^{-0.54}\left(\frac{L_{sc}}{L_{sat}}\right)$	HFE 7100 D_h = 0.176 – 0.416 mm G = 670 – 5550 kg/m^{2}s p = 113.8 kPa q'' < 664 W/cm^2
Baburajan *et al.* (2013) [69]	$\phi_{sc}^2 = 1 + 32500Bo^{1.6}Ja*^{-1.2}\left(\frac{D\times 10^3}{9.53}\right)^{2.2}$	Water D = 5.5 – 9.5 mm G = 450 – 935 kg/m^{2}s p = 120 kPa q'' < 50 W/cm^2
Yan *et al.* (2017) [70]	$\phi_{sc}^2 = 1 + 2250Bo^{1.5}Ja*^{-1.43}\left(\frac{\rho_f}{\rho_g}\right)^{0.2}$	Water D = 9 mm G = 6000 – 10000 kg/m^{2}s p = 3000 – 5000 kPa q'' < 1250 W/cm^2
Ramesh & Gedupudi (2019) [71]	For non-circular channels with $Bo > 10^{-4}$, $\phi_{sc}^2 = 1 + 6.86Bo^{1.595}Ja*^{-1.44}L^{5.046}D_h^{-3.179}$	D_h = 0.435 – 0.74 mm G = 77 – 1188 kg/m^{2}s p = 101.3 kPa q'' < 110 W/cm^2 $\Delta T_{sub,in}$ = 30 – 70 °C L = 0.03, 0.04 m
	For non-circular channels with $Bo \le 10^{-4}$, $\phi_{sc}^2 = 1 + Bo(4.38\times 10^7 Bo - 5776.7)$	D_h = 0.94 mm G = 200 – 500 kg/m^{2}s p = 101.3 kPa q'' < 4 W/cm^2 $\Delta T_{sub,in}$ = 10 °C L = 0.08 m
	For circular tubes with $25 \le L/D \le 50$, $\phi_{sc}^2 = 1 + 4.86\times 10^6 Bo^{2.4657}\left(\frac{L}{L_{sat}}\right)^{1.9505}Ja*^{-2.1436}$	D = 1.05 – 2.44 mm G = 3000 – 45000 kg/m^{2}s p = 200 – 1600 kPa q'' < 8000 W/cm^2 T_{in} = 22 – 63 °C L = 0.025 – 0.125 m
	For circular tubes with $L/D < 25$, $\phi_{sc}^2 = \left(\frac{L}{L_{sat}}\right)^{0.4895}\exp\left(\frac{L}{L_{sat}}+0.9169\right)$	D = 8 mm G = 5000 – 10000 kg/m^{2}s p = 2500 kPa q'' < 1400 W/cm^2 T_{in} = 30 – 60 °C L = 0.1 m
Ma *et al.* (2024) [64]	$\phi_{sc}^2 = \left[1 + 0.44\frac{Bd^{0.33}}{X^{1.3}P_r^{0.86}}\right]\frac{\mathrm{Re}_f^{0.1}We_{fo}^{0.2}}{\left[1+(\rho_f/\rho_g)^{0.625}Ja*\right]^{0.53}}$	Water, R134a, CO_2, R236fa, R245fa, HFE 7100, R1234yf, R1233zd(E), R1234ze(E), acetone, R600a D_h = 0.1 – 2.6 mm G = 50 – 3000 kg/m^{2}s p = 101 – 3970 kPa q'' < 400 W/cm^2 ΔT_{sub} = 5 – 75 °C

learning rule. The Adam [81] learning algorithm is well suited for convergence of multilayer neural networks and is employed as the learning rule. The loss is calculated, and the weights and biases are updated at the end of each iteration, consisting of n observations. Mini-Batch Gradient Descent (MBGD) is used in the present study, where the mini-batch size, n, is between 1 and N, the total number of observations. During MBGD, the number of iterations per *epoch,* which corresponds to the passing of the entire database through the training process, is obtained by truncating N/n. At the end of each epoch, leftover training data are skipped, and the observations used in each iteration are shuffled to ensure same observations are not excluded from training in each iteration.

Table 7
Mean absolute errors (%) of seminal correlations for ϕ_{sc}^2 used to predict pressure drop of subcooled flow boiling.

Correlation	Total (1065 data points)	Single-sided (393 data points)	Double-sided (672 data points)	$\Delta T_{sub,in} < 10°C$ (415 data points)	$\Delta T_{sub,in} \geq 10°C$ (650 data points)	$G < 1200$ kg/m^{2}s (144 data points)	$G \geq 1200$ kg/m^{2}s (921 data points)
Owens & Schrock (1960) [65]	38.7	38.3	38.9	40.7	38.1	67.1	35.1
Tarasova *et al.* (1966) [66]	182.6	113.7	226.6	497.8	95.1	368.0	157.9
Hahne *et al.* (1993) [67], $C = 80$	34.1	33.2	34.6	42.7	31.4	67.0	30.0
Hahne *et al.* (1993) [67], $C = 500$	53.4	33.8	65.6	43.6	55.3	50.4	53.8
Tong *et al.* (1997) [68], $C = 1.35$	55.8	72.2	45.6	36.4	60.7	52.8	56.2
Tong *et al.* (1997) [68], $C = 0.4$	81.3	87.2	77.5	70.7	84.7	80.6	81.4
Kim & Mudawar (2012) [36]	57.3	66.3	51.9	180.9	47.5	70.7	55.4
Baburajan *et al.* (2013) [69]	54.4	69.9	45.4	61.4	53.2	54.2	54.5
Yan *et al.* (2017) [70]	77.4	93.4	68.1	125.5	71.6	58.7	79.8
Ramesh & Gedupudi (2019) [71]	70.5	86.3	61.4	106.9	65.6	62.3	71.6

To ensure the ANN does not become overtrained, where it loses generality to data not used in the training process, the database is randomly divided into three subsets. The majority of the database, accounting for 70%, is *training data*, used to train the model. The remaining data is withheld from training and is split into two subsets, each accounting for 15% of the entire database. The *testing data* is used to assess the accuracy of the model at the conclusion of training. All reported statistics and accuracy of the model are based on testing data. The validation data is comprised of the remaining data and is used to obviate over training. At the end of each iteration, the loss of the validation data is calculated. A validation patience is set to stop training after the loss of the validation does not improve after a set number of iterations. The validation patience is reported as a number of epochs in the present study.

5.2. Development of ANN

Due to pressure measurements for FBM's heated section only being

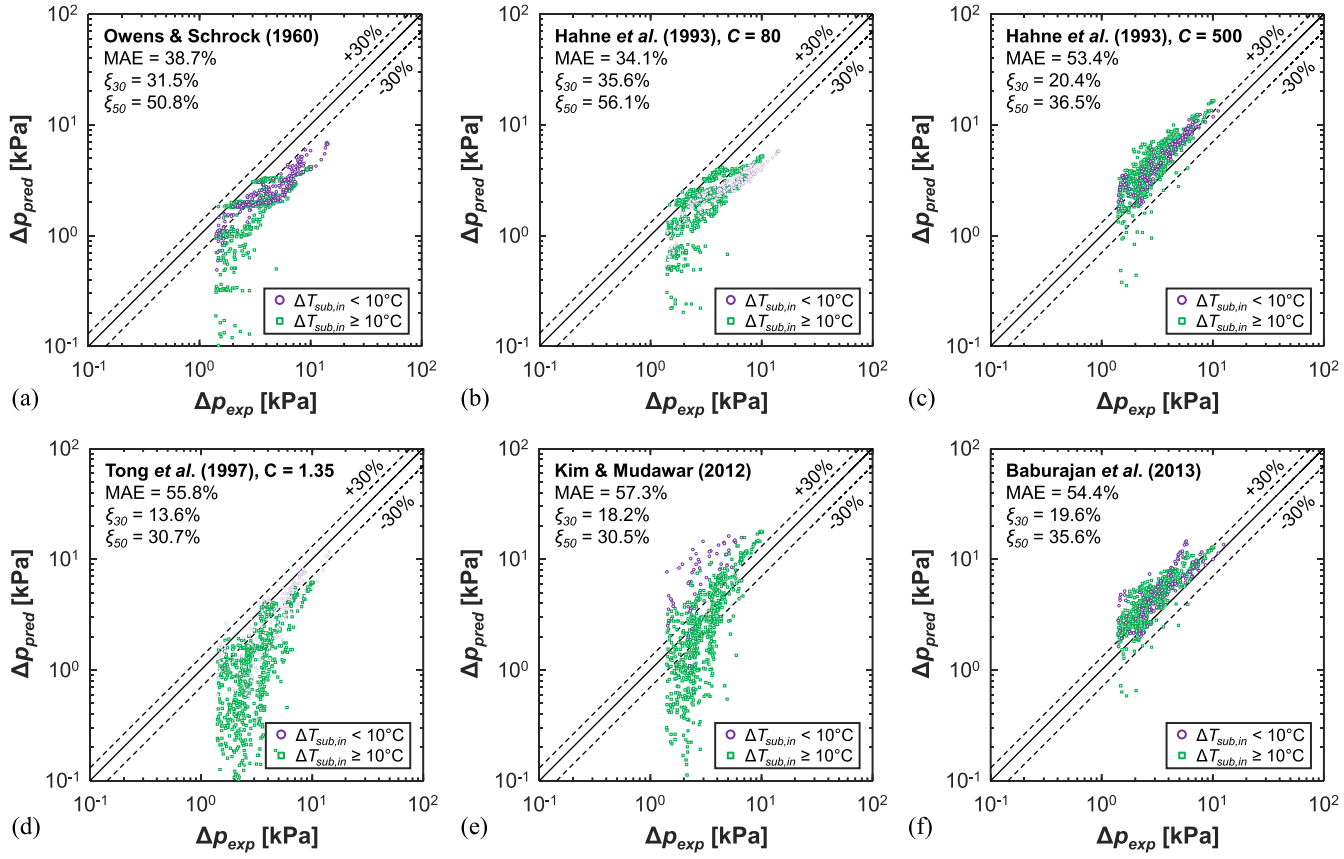

Fig. 11. Parity plots assessing the predictive performance of correlations for subcooled flow boiling pressure drop: (a) Owens & Schrock (1960), (b) Hahne *et al.* (1993) with $C = 80$, (c) Hahne *et al.* (1993) with $C = 500$, (d) Tong *et al.* (1997) with $C = 1.35$, (e) Kim & Mudawar (2012), and (f) Baburajan *et al.* (2013).

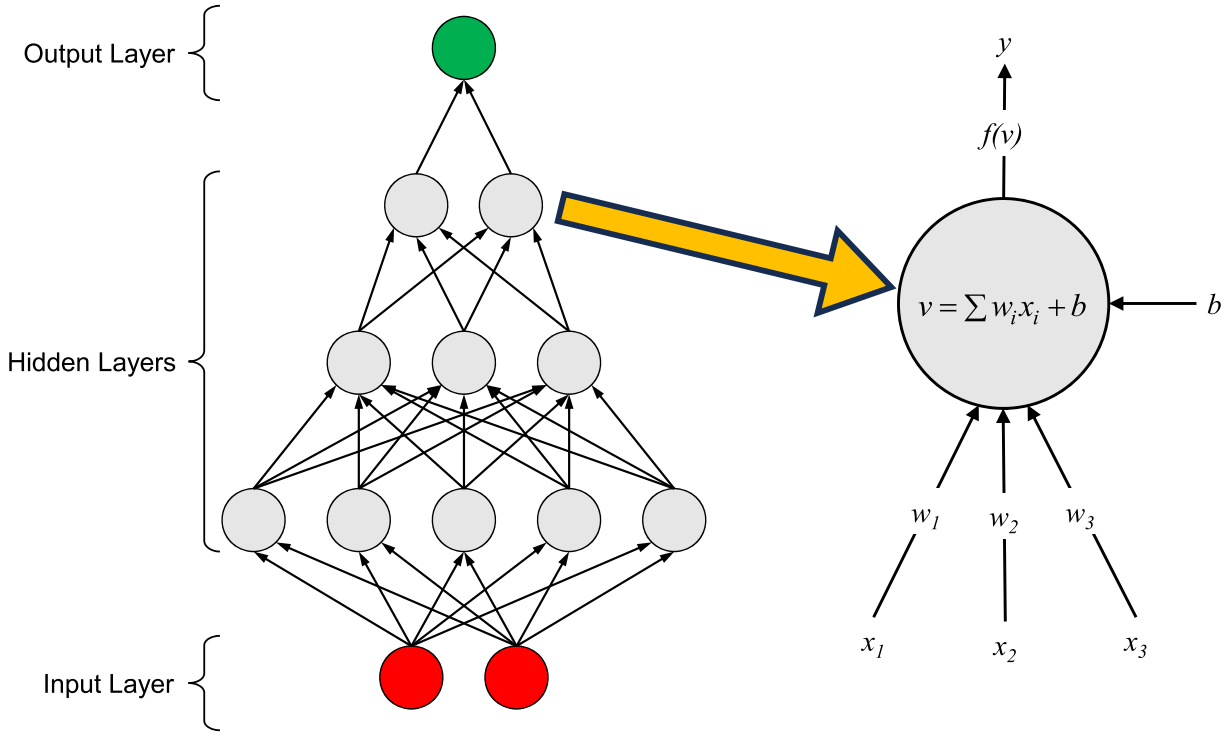

Fig. 12. Schematic displaying the interlinking structure of a fully connected, feed forward Artificial Neural Network, ANN, and the function of a neuron including the inputs, x_i, corresponding weight applied to each input, w_i, bias, b, input to activation function, v, activation function, $f(v)$, and output, y.

recorded at the inlet and outlet, Δp_{tot} is chosen as the desired output parameter to avoid assuming a linear pressure gradient, *e.g.*, $dp/dz = (p_{out} - p_{in})/L_h$. This encompasses the Δp attributed to friction and acceleration, which can be difficult to quantify due to nonequilibrium observed in the channel [21,25]. The selection of input parameters is not as straight forward, and there is no universal standard to determine the optimal set of input parameters. A review of various ANN applications calls for a systematic methodology relying on an expertise in the subject matter, and either a systematic or statistical assessment of relevant parameters [72]. Assessing the various correlations presented in Tables 3, 4, and 6 reveals that relevant parameters affecting Δp can be categorized as operating conditions (G, p, x, q''_w), channel dimensions (D_h, D_e, P_h, P_f), and fluid properties (ρ, μ, σ, h_{fg}). To facilitate a model predicting total Δp across the channel, inlet conditions are relied upon, as compared to correlations which rely on the determination of local parameters via numerical scheme coupling conservations mass, momentum, and energy. Additionally, information regarding the single-phase and two-phase length of the channel is required which is implicitly provided by the inclusion of inlet subcooling, $\Delta T_{sub,in}$, and length, L (which is equal to the heated length, L_h), along with other included parameters (G, p_{in}, q''_w, P_h).

The influence and importance of these parameters are assessed in Fig. 13. Pearson's correlation coefficient (r) is used to assess the linear correlation between two parameters, which, for any two parameters A and B is calculated as

$$r(A,B) = \frac{1}{N-1}\sum_{i=1}^{N}\left(\frac{A_i - \mu_A}{\sigma_A}\right)\left(\frac{B_i - \mu_B}{\sigma_B}\right). \quad (28)$$

Values are bound by -1 and 1, which represent a negative and positive linear correlation, respectively, and values near 0 indicate no linear dependence. Fig. 13(a) depicts the corresponding r for each pair of relevant parameters, including the dependent variable Δp. The size and color of each circle respectively indicate the magnitude and exact value of r. Examining the values of r depicted in Fig. 13(a) reveals the fluid properties are strongly correlated to p_{in}, values such as D_h, P_f, and L are constant and do not affect the database, and D_e and P_h are strongly correlated because $D_e = 4A_c/P_h$. These conclusions justify that p_{in} is sufficient to capture the influence of various fluid properties, D_h, P_f, and L are irrelevant, and only either D_e or P_h is needed. Irrelevant or redundant parameters are removed from the database, and the remaining parameters are assessed via *F-Test* to determine the statistical significance of each parameter on Δp. *F-Test* is a hypothesis test to assess probability that the response values grouped by predictor variables come from populations with the same mean. *p-value* (probability value), φ, describes the probability that the *null hypothesis* is true, and the variable is statistically insignificant. Null hypothesis is generally rejected when $\varphi < 0.05$ [82]. Fig. 13(b) depicts the *F-Test* result for key variables as $-\ln(\varphi)$, where values > 3 correspond to $\varphi < 0.05$, indicating statistical importance. Each remaining variable demonstrates statistical significance in determining Δp, and should be included as an input to the ANN.

Due to the limitation of the present database, some values with a known influence on Δp were eliminated, such as D_h and L. To account for these crucial variables and better generalize the ANN, the inputs and outputs of the ANN are nondimensionalized. Bejan number, Be, is selected as dimensionless Δp, and serves as the output of the ANN. Table 8 lists a variety of dimensionless groups that capture relevant parameters in Fig. 13(b). Numerous ANNs were trained using the MATLAB Deep Learning Toolbox [83] to assess various combinations of the dimensionless inputs and training parameters listed in Table 8, and the ANN yielding the lowest MAE is chosen as the finalized model. Training parameters that were selected for optimization are network architecture, mini-batch size, initial learn rate, and validation patience, while others were set as default parameters recommended for Adam [81] or recommended in previous studies discussed in section 5.1. Considered architectures were constructed such that the final hidden layer's size is fixed at 10 neurons, and each hidden layer has 10 more neurons than the subsequent layer. For example, a network of 7 hidden layers has an architecture of {70 – 60 – 50 – 40 – 30 – 20 – 10}.

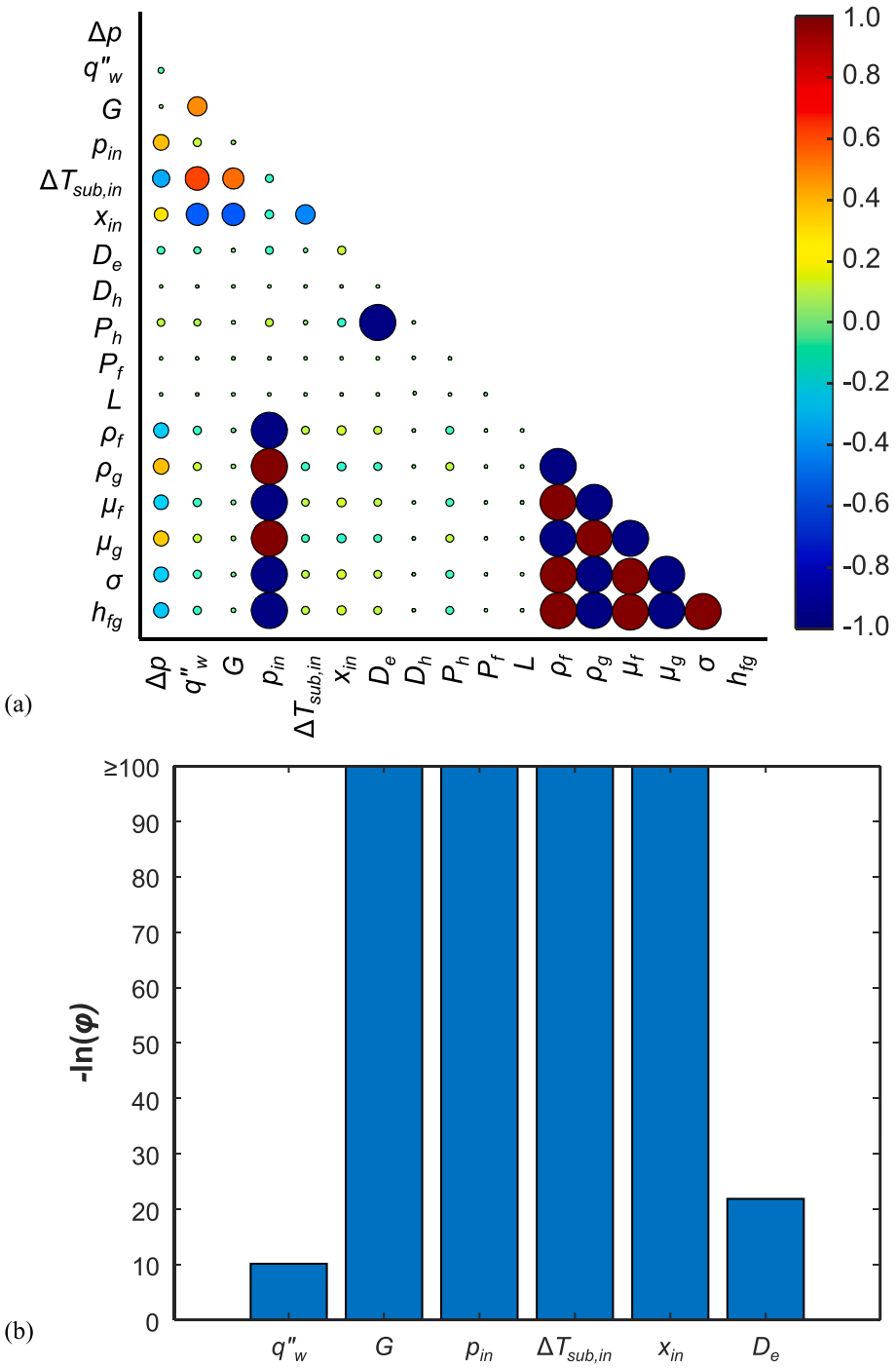

Fig. 13. (a) Pearson's correlation coefficients (r) for relevant input parameters: pressure drop (Δp), wall heat flux (q''_w), mass velocity (G), inlet pressure (p_{in}), degree of inlet subcooling ($\Delta T_{sub,in}$), flow quality (x_{in}), equivalent heated diameter (D_e), hydraulic diameter (D_h), heated perimeter (P_h), friction perimeter (P_f), channel length (L), density of liquid (ρ_f) and vapor (ρ_g), dynamic viscosity of liquid (μ_f) and vapor (μ_g), surface tension (σ), and latent heat of vaporization (h_{fg}). The size of each circle represents the strength of correlation (with larger circles meaning stronger correlation), and the color represents the actual value of r. (b) F-Test results for relevant parameters.

5.3. Results of the Trained ANN

5.3.1. Predictive Accuracy of the ANN

Table 8 contains the finalized set of inputs and various parameters chosen during the training process. The optimized ANN predicted the testing subset of the database with an overall MAE of 5.2%. Figs. 14(a-d) depict parity plots for single-side heating with subcooled inlet, double-sided heating with subcooled inlet, single-sided heating with saturated inlet, and double-sided heating with saturated inlet, respectively. Each portion of the database is predicted with good accuracy. For each subset, at least 95.5% of the data is predicted within ±30% error, and 98.5% is predicted within ±50% error. The MAE is highest during single-sided heating with subcooled inlet, which is explained both by the prevalence of flow instabilities observed during these operating conditions [21] and thermodynamic nonequilibrium. Nonetheless, the ANN predicts Δp with relatively high accuracy compared to other prediction methods, MAE = 9.7%, owed to the ANN's ability to capture the influence of unique and complex phenomena inherent to the data.

Table 8
Parameters used for training neural networks.

Parameter	Range Tested	Finalized Model
Max Epochs	5000	5000
L2 Regularization	0.0001	0.0001
Gradient Decay Factor	0.9	0.9
Squared Gradient Decay Factor	0.999	0.999
Denominator Offset	1×10^{-8}	1×10^{-8}
Mini-batch Size, n	8 – 512	64
Learning Rate	0.0001 – 0.01	0.001
Validation Patience	1 – 50	25
Hidden Layers	1 – 20	6
Input Parameters	$Bo, x_e, Ja*, x, \mathrm{Re}_{fo}, \mathrm{Re}_{go}, We_{fo}, We_{go}, p_r, \frac{\rho_g}{\rho_f}, Su_{fo}, Su_{go}, \frac{D_e}{D_h}, \frac{D_h}{L}, \frac{D_e}{L}$	$Bo, Ja*, x, \mathrm{Re}_{fo}, \mathrm{Re}_{go}, We_{fo}, \frac{\rho_g}{\rho_f}, Su_{go}, \frac{D_e}{L}$

5.3.2. *Predicted Parametric Trends of the ANN*

While the ANN displays excellent predictive accuracy for the entire database, it is not guaranteed to capture physical trends. Because ANNs are trained to minimize the loss of the training data, they tend to capture empirical trends inherent to the training data, but do not have a set form which biases the results to conform to physical trends; for example, Δp increasing with increasing G. To assess the ANN's reliability in capturing physical parametric trends, it is retrained while withholding select data

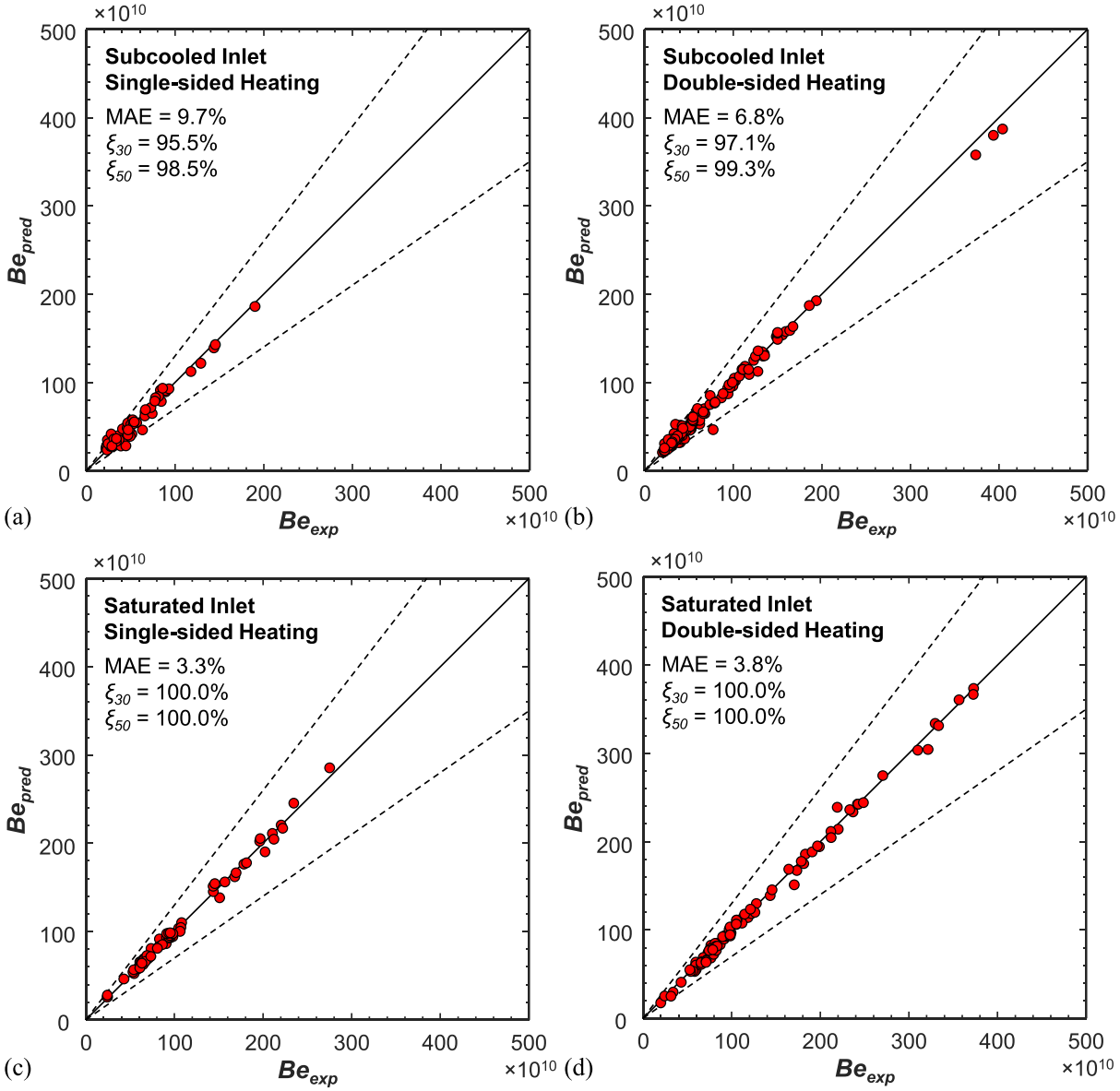

Fig. 14. Parity plots of the final ANN's predictions for subcooled inlet conditions with (a) single- and (b) double-sided heating and saturated inlet conditions with (c) single- and (d) double-sided heating. The ANN's prediction accuracy is assessed by a combination of mean absolute error (MAE) and statistical inliers within ±30% (ξ_{30}) and ±50% (ξ_{50}) of experimental values.

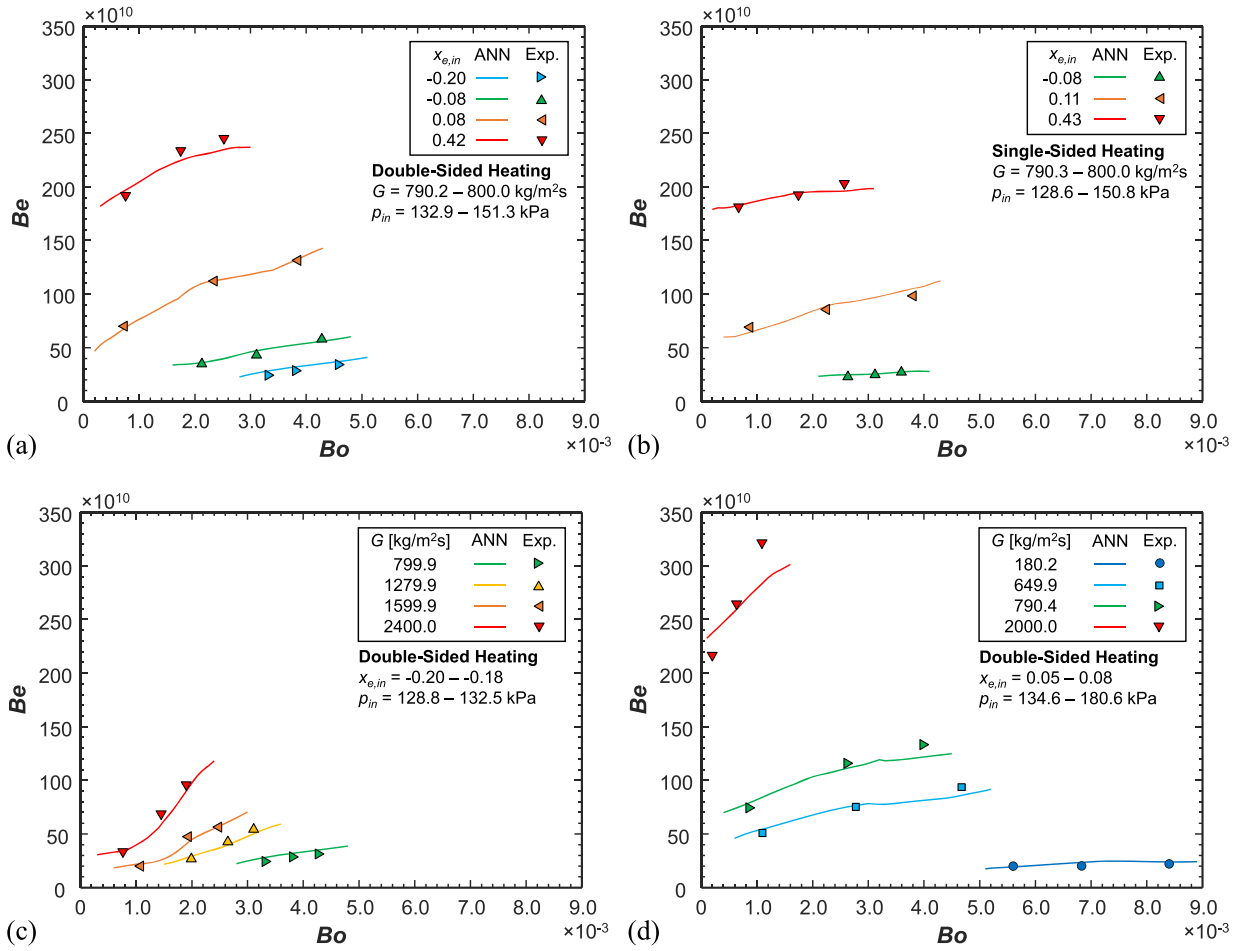

Fig. 15. Parametric trends of Bejan number, *Be,* with respect to Boiling number, *Bo*, predicted by the ANN compared to corresponding data excluded from training. Each plot shows predictions for (a) double-sided and (b) single-sided heating at constant mass velocity, $G \approx 800$ kg/m^{2}s, and different inlet thermodynamic equilibrium qualities, $x_{e,in}$ and during double-sided heating at different G for (c) $x_{e,in} \approx -0.20$ and (d) $x_{e,in} \approx 0.05$.

from the training process. Fig. 15 shows the predicted trends of the ANN compared to data excluded during training. Predicted parametric trends during double-sided heating for $G \approx 800$ kg/m^{2}s at different $x_{e,in}$ are presented in Fig. 15(a). The model predicts increasing *Be* with increasing *Bo* and $x_{e,in}$, as observed the testing data. Increasing *Bo* and $x_{e,in}$ result in greater vapor production, which increases the accelerational Δp component, resulting in greater Δp. Similar trends are captured for near-identical operating conditions but with single-sided heating in Fig. 15 (b). However, one difference observed in both the predictions by the ANN and the testing data, is the milder increase of *Be* with respect to *Bo* than that observed during double-sided heating. This again can be attributed to greater vapor production, which occurs from twice the heat added to the fluid for the same q''_w in double-sided compared to single-sided heating. Fig. 15(c) presents trends for $x_{e,in} \approx -0.19$ at different G during double-sided heating. The ANN captures the trend of increasing *Be* with increasing G and, for each G, increasing *Bo*. Fig. 15(d) focuses on trends of *Be* with respect to *Bo* during double sided heating with $x_{e,in} \approx 0.05$ and different G. The ANN captures the expected trend of *Be* increasing with G, similar to that observed in Fig. 15(c). *Be* monotonically increases with G and q''_w and, as observed in Figs. 15(a) and 15 (b), *Be* is greater for higher $x_{e,in}$. The only trend not captured well is the behavior for $G = 2000$ kg/m^2 in Fig. 15(d).

6. Conclusions

This study explored the pressure drop (Δp) characteristics of flow boiling of nPFH in a rectangular channel in microgravity. The experiments were performed onboard the ISS as part of FBCE to amass a large database of 3393 Δp datapoints. Firstly, the parametric effects on flow boiling Δp are explored; the operating parameters explored include mass velocity (180.0 – 3200.1 kg/m^{2}s), inlet quality (-0.62 – 0.87), inlet pressure (119.6 – 200.4 kPa), wall heat flux (< 55.1 W/cm^2), and heating configuration (one or two channel walls heated). Secondly, several prediction techniques in the form of seminal models/correlations and machine learning tools are assessed using 2478 datapoints (with lesser experimental uncertainties) and recommendations provided. Key conclusions are as follows:

(i) Δp typically increases with increasing mass velocity, increasing inlet quality (for fixed mass velocity), and increasing heat flux (until a point after which it plateaus). The primary reason for most of these physical trends is flow acceleration increasing bulk flow velocities and both frictional and accelerational components of Δp. At similar heat fluxes, Δp is relatively higher for double-sided heating when compared to single-sided due to the higher amount of heat added to the fluid. Inlet pressure did not have an appreciable effect on Δp.

(ii) μg_e flow boiling was prone to dynamic two-phase flow instabilities, which induced severe periodic oscillations in inlet pressure and Δp, which occasionally exceeded the time-averaged values.

(iii) 1099 purely saturated flow boiling datapoints were used to assess 7 mixture viscosity models used with the Homogeneous Equilibrium Model (HEM) and 17 empirical correlations used with the

Separated Flow Model (SFM). Of these, the original SFM approach proposed by Lockhart and Martinelli [48] was most accurate with a 17.1% MAE. Both Lockhart and Martinelli [48] and Mishima and Hibiki's [49] correlations yielded the narrowest scatter of predictions with > 97% of datapoints predicted within ±50%, while the others have larger scatter. The best HEM predictions were provided using Owens' [41] relation, which is simply equal to the liquid viscosity at all qualities, with a 26.7% MAE and 90% of datapoints predicted within ±50%. Both the HEM and SFM predict the $G < 1200$ kg/m^{2}s data with far better accuracy than high G.

(iv) 1065 purely subcooled flow boiling datapoints were used to assess 9 seminal correlations. The most accurate predictions were made by the correlation by Hahne *et al.* [67] with empirical constant $C = 80$, evidenced by a 34.1% MAE with 56.1% of datapoints predicted within ±50%. Predicted trends show this correlation would yield even more accurate predictions if C were appropriately tuned for nPFH.

(v) Comparing the performance of seminal models/correlations for saturated versus subcooled flow boiling, both the HEM and SFM predict saturated boiling Δp better than the correlations available for subcooled boiling Δp. The foremost reason is subcooled boiling having received lesser research attention compared to saturated boiling, so fewer Δp_{sc} are available, none of which are directly applicable to the operating conditions in this study.

(vi) An ANN of the fully connected, feed-forward type, and having 6 hidden layers, was developed. Statistical analysis of data revealed the input parameters paramount for flow boiling Δp and optimized the model parameters and options. The entire database was randomly divided into three subsets: 70% training data, 15% testing data, and 15% validation data. The ANN was trained using Adam to predict Δp. It accurately predicted the testing subset of the entire database with a 5.24% MAE, while conforming to expected physical trends in previously unseen data. The developed ANN's predictive performance is far better than any existing empirical correlation, demonstrating its superior capability of serving as a prediction tool for Δp.

Data availability

The experimental raw data used in this paper is publicly available in a NASA repository. The ANN is provided as supplementary material.

CRediT authorship contribution statement

Issam Mudawar: Writing – original draft, Visualization, Validation, Supervision, Project administration, Methodology, Investigation, Funding acquisition, Formal analysis, Data curation, Conceptualization. **Steven J. Darges:** Writing – review & editing, Writing – original draft, Visualization, Validation, Software, Methodology, Investigation, Formal analysis, Data curation, Conceptualization. **V.S. Devahdhanush:** Writing – review & editing, Writing – original draft, Visualization, Validation, Methodology, Investigation, Formal analysis, Data curation, Conceptualization. **Mohammad M. Hasan:** Writing – review & editing, Supervision, Project administration, Funding acquisition, Data curation. **Henry K. Nahra:** Writing – review & editing, Supervision, Project administration, Funding acquisition, Data curation. **R. Balasubramaniam:** Writing – review & editing, Data curation. **Jeffrey R. Mackey:** Writing – review & editing, Visualization, Data curation.

Declaration of competing interest

The authors declare the following financial interests/personal relationships which may be considered as potential competing interests: Issam Mudawar reports financial support was provided by NASA. Mohammad M. Hasan, Henry K. Nahra reports a relationship with NASA that includes: employment. If there are other authors, they declare that they have no known competing financial interests or personal relationships that could have appeared to influence the work reported in this paper.

Acknowledgement

The authors appreciate the support of the National Aeronautics and Space Administration (NASA) under grant no. 80NSSC22K0328. The authors thank the FBCE personnel at NASA Glenn Research Center, Cleveland, Ohio, especially Nancy Hall (FBCE Project Manager), Rochelle May, Phillip Gonia, Jose Lombay-Gonzalez (Software Engineering), Mark Sorrells (Assembly, Integration and Test Lead), Jesse DeFiebre (Fluids Lead), Monica Guzik (FBCE Chief Engineer), and ZIN FCF Mission Operations Team, for their dedicated technical assistance and successful completion of ISS testing.

Supplementary materials

Supplementary material associated with this article can be found, in the online version, at doi:10.1016/j.ijheatmasstransfer.2024.126593.

References

[1] F.P. Chiaramonte, J. McQuillen, H.K. Nahra, P. Manoharan, H. Vanhala, B.J. Motil, J. Kim, V. Carey, W.G. Anderson, J. Plawsky, L. Carter, A. Jackson, 2019 NASA division of space and life and physical sciences research and applications fluid physics workshop report, NASA/CP-20205001256, NASA Glenn Research Center, Cleveland, OH, USA, 2020.

[2] T.J. LaClair, I. Mudawar, Thermal transients in a capillary evaporator prior to the initiation of boiling, Int. J. Heat Mass Transfer 43 (21) (2000) 3937–3952, https://doi.org/10.1016/S0017-9310(00)00042-9.

[3] G. Liang, I. Mudawar, Pool boiling critical heat flux (CHF) – Part 2: Assessment of models and correlations, Int. J. Heat Mass Transfer 117 (2018) 1368–1383, https://doi.org/10.1016/j.ijheatmasstransfer.2017.09.073.

[4] I. Mudawar, R.A. Houpt, Mass and momentum transport in smooth falling liquid films laminarized at relatively high Reynolds numbers, Int. J. Heat Mass Transfer 36 (14) (1993) 3437–3448, https://doi.org/10.1016/0017-9310(93)90162-Y.

[5] S. Mukherjee, I. Mudawar, Pumpless loop for narrow channel and micro-channel boiling, J. Electron. Packag. 125 (3) (2003) 431–441, https://doi.org/10.1115/1.1602708.

[6] M.E. Johns, I. Mudawar, An ultra-high power two-phase jet-impingement avionic clamshell module, J. Electron. Packag. 118 (4) (1996) 264–270, https://doi.org/10.1115/1.2792162.

[7] W.P. Klinzing, J.C. Rozzi, I. Mudawar, Film and transition boiling correlations for quenching of hot surfaces with water sprays, J. Heat Treat. 9 (2) (1992) 91–103, https://doi.org/10.1007/BF02833145.

[8] M.K. Sung, I. Mudawar, Single-phase and two-phase heat transfer characteristics of low temperature hybrid micro-channel/micro-jet impingement cooling module, Int. J. Heat Mass Transfer 51 (15–16) (2008) 3882–3895, https://doi.org/10.1016/j.ijheatmasstransfer.2007.12.016.

[9] M.K. Sung, I. Mudawar, Single-phase and two-phase hybrid cooling schemes for high-heat-flux thermal management of defense electronics, J. Electron. Packag. 131 (2) (2009) 021013, https://doi.org/10.1115/1.3111253.

[10] Y. Ma, J.N. Chung, An experimental study of forced convection boiling in microgravity, Int. J. Heat Mass Transfer 41 (15) (1998) 2371–2382.

[11] D.M. Iceri, G. Zummo, L. Saraceno, G. Ribatski, Convective boiling heat transfer under microgravity and hypergravity conditions, Int. J. Heat Mass Transfer 153 (2020) 119614, https://doi.org/10.1016/j.ijheatmasstransfer.2020.119614.

[12] C. Konishi, I. Mudawar, Review of flow boiling and critical heat flux in microgravity, Int. J. Heat Mass Transfer 80 (2015) 469–493, https://doi.org/10.1016/j.ijheatmasstransfer.2014.09.017.

[13] P. Di Marco, W. Grassi, Pool boiling in microgravity: Assessed results and open issues, in: Proceedings of 3rd European Thermal-Sciences Conference, Heidelberg, Germany, 2000, pp. 81–90.

[14] R. Raj, J. Kim, J. McQuillen, Pool Boiling Heat Transfer on the International Space Station: Experimental Results and Model Verification, J. Heat Transfer 134 (10) (2012) 101504, https://doi.org/10.1115/1.4006846.

[15] V.K. Dhir, G.R. Warrier, E. Aktinol, D. Chao, J. Eggers, W. Sheredy, W. Booth, Nucleate pool boiling experiments (NPBX) on the International Space Station, Microgravity Sci. Technol. 24 (5) (2012) 307–325, https://doi.org/10.1007/s12217-012-9315-8.

[16] G.R. Warrier, V.K. Dhir, D.F. Chao, Nucleate pool boiling experiment (NPBX) in microgravity: International Space Station, Int. J. Heat Mass Transfer 83 (2015) 781–798, https://doi.org/10.1016/j.ijheatmasstransfer.2014.12.054.

[17] H. Ohta, H. Asano, O. Kawanami, K. Suzuki, R. Imai, Y. Shinmoto, S. Matsumoto, T. Kurimoto, H. Takaoka, K. Fujii, M. Sakamoto, K. Sawada, H. Kawasaki, A. Okamoto, K. Kogure, T. Oka, K. Usuku, T. Tomobe, M. Takayanagi, Development of boiling and two-phase flow experiments on board ISS (Research

objectives and concept of experimental setup), Int. J. Microgravity Sci. Appl. 33 (1) (2016) 330101, https://doi.org/10.15011/ijmsa.33.330102.
[18] K. Inoue, H. Ohta, Y. Toyoshima, H. Asano, O. Kawanami, R. Imai, K. Suzuki, Y. Shinmoto, S. Matsumoto, Heat loss analysis of flow boiling experiments onboard International Space Station with unclear thermal environmental conditions (1st Report: Subcooled liquid flow conditions at test section inlet), Microgravity Sci. Technol. 33 (2) (2021) 28, https://doi.org/10.1007/s12217-021-09869-5.
[19] K. Inoue, H. Ohta, H. Asano, O. Kawanami, R. Imai, K. Suzuki, Y. Shinmoto, T. Kurimoto, S. Matsumoto, Heat loss analysis of flow boiling experiments onboard International Space Station with unclear thermal environmental conditions (2nd Report: Liquid-vapor two-phase flow conditions at test section inlet), Microgravity Sci. Technol. 33 (5) (2021) 57, https://doi.org/10.1007/s12217-021-09902-7.
[20] P. Chorin, A. Boned, J. Sebilleau, C. Colin, O. Schoele-Schulz, N. Picchi, C. Schwarz, B. Toth, D. Mangini, Conception of a compact flow boiling loop for the International Space Station- First results in parabolic flights, Comptes Rendus. Mécanique 351 (S2) (2023) 1–20, https://doi.org/10.5802/crmeca.147.
[21] I. Mudawar, V.S. Devahdhanush, S.J. Darges, M.M. Hasan, H.K. Nahra, R. Balasubramaniam, J.R. Mackey, Heat transfer and interfacial flow physics of microgravity flow boiling in single-side-heated rectangular channel with subcooled inlet conditions – Experiments onboard the International Space Station, Int. J. Heat Mass Transfer 207 (2023) 123998, https://doi.org/10.1016/j.ijheatmasstransfer.2023.123998.
[22] V.S. Devahdhanush, I. Mudawar, H.K. Nahra, R. Balasubramaniam, M.M. Hasan, J. R. Mackey, Experimental heat transfer results and flow visualization of vertical upflow boiling in Earth gravity with subcooled inlet conditions – In preparation for experiments onboard the International Space Station, Int. J. Heat Mass Transfer 188 (2022) 122603, https://doi.org/10.1016/j.ijheatmasstransfer.2022.122603.
[23] S.J. Darges, V.S. Devahdhanush, I. Mudawar, H.K. Nahra, R. Balasubramaniam, M. M. Hasan, J.R. Mackey, Experimental results and interfacial lift-off model predictions of critical heat flux for flow boiling with subcooled inlet conditions – In preparation for experiments onboard the International Space Station, Int. J. Heat Mass Transfer 183 (2022) 122241, https://doi.org/10.1016/j.ijheatmasstransfer.2021.122241.
[24] V.S. Devahdhanush, S.J. Darges, I. Mudawar, H.K. Nahra, R. Balasubramaniam, M. M. Hasan, J.R. Mackey, Flow visualization, heat transfer, and critical heat flux of flow boiling in Earth gravity with saturated liquid-vapor mixture inlet conditions – In preparation for experiments onboard the International Space Station, Int. J. Heat Mass Transfer 192 (2022) 122890, https://doi.org/10.1016/j.ijheatmasstransfer.2022.122890.
[25] I. Mudawar, V.S. Devahdhanush, S.J. Darges, M.M. Hasan, H.K. Nahra, R. Balasubramaniam, J.R. Mackey, Effects of heating configuration and operating parameters on heat transfer and interfacial physics of microgravity flow boiling with subcooled inlet conditions – Experiments onboard the International Space Station, Int. J. Heat Mass Transfer 217 (2023) 124732, https://doi.org/10.1016/j.ijheatmasstransfer.2023.124732.
[26] I. Mudawar, V.S. Devahdhanush, S.J. Darges, M.M. Hasan, H.K. Nahra, R. Balasubramaniam, J.R. Mackey, Microgravity flow boiling experiments with liquid-vapor mixture inlet onboard the International Space Station, Int. J. Heat Mass Transfer 224 (2024) 125299, https://doi.org/10.1016/j.ijheatmasstransfer.2024.125299.
[27] I. Mudawar, S.J. Darges, V.S. Devahdhanush, Parametric experimental trends, interfacial behavior, correlation assessment, and interfacial lift-off model predictions of critical heat flux for microgravity flow boiling with subcooled inlet conditions – Experiments onboard the International Space Stat, Int. J. Heat Mass Transfer 213 (2023) 124296, https://doi.org/10.1016/j.ijheatmasstransfer.2023.124296.
[28] I. Mudawar, S.J. Darges, V.S. Devahdhanush, Critical heat flux for flow boiling with saturated two-phase inlet in microgravity onboard the International Space Station, Int. J. Heat Mass Transfer (2024) under minor revision.
[29] V.S. Devahdhanush, I. Mudawar, Subcooled flow boiling heat transfer in a partially-heated rectangular channel at different orientations in Earth gravity, Int. J. Heat Mass Transfer 195 (2022) 123200, https://doi.org/10.1016/j.ijheatmasstransfer.2022.123200.
[30] S.J. Darges, V.S. Devahdhanush, I. Mudawar, Assessment and development of flow boiling critical heat flux correlations for partially heated rectangular channels in different gravitational environments, Int. J. Heat Mass Transfer 196 (2022) 123291, https://doi.org/10.1016/j.ijheatmasstransfer.2022.123291.
[31] I. Mudawar, S.J. Darges, V.S. Devahdhanush, Prediction technique for flow boiling heat transfer and critical heat flux in both microgravity and Earth gravity via artificial neural networks (ANNs), Int. J. Heat Mass Transfer 220 (2024) 124998, https://doi.org/10.1016/j.ijheatmasstransfer.2023.124998.
[32] W.A. Arnold, T.G. Hartman, J. McQuillen, Chemical characterization and thermal stressing studies of perfluorohexane fluids for space-based applications, J. Spacecr. Rockets 44 (1) (2007) 94–102, https://doi.org/10.2514/1.22537.
[33] E.W. Lemmon, I.H. Bell, M.L. Huber, M.O. McLinden, in: NIST Standard Reference Database 23: Reference Fluid Thermodynamic and Transport Properties-REFPROP, Version 10, NIST, Gaithersburg, MD, USA, 2018.
[34] J. Lee, V.S. Devahdhanush, S.J. Darges, I. Mudawar, Effects of flow loop compressible volume position on system instabilities during flow boiling in micro-channel heat sinks, Int. J. Heat Mass Transfer 198 (2022) 123394, https://doi.org/10.1016/j.ijheatmasstransfer.2022.123394.
[35] I. Mudawar, S.J. Darges, V.S. Devahdhanush, M.M. Hasan, H.K. Nahra, R. Balasubramaniam, J.R. Mackey, Two-phase flow instabilities during microgravity flow boiling onboard the International Space Station, Int. J. Heat Mass Transfer 234 (2024) 126102, https://doi.org/10.1016/j.ijheatmasstransfer.2024.126102.
[36] S.M. Kim, I. Mudawar, Consolidated method to predicting pressure drop and heat transfer coefficient for both subcooled and saturated flow boiling in micro-channel heat sinks, Int. J. Heat Mass Transfer 55 (13–14) (2012) 3720–3731, https://doi.org/10.1016/j.ijheatmasstransfer.2012.02.061.
[37] V.S. Devahdhanush, S. Lee, I. Mudawar, Consolidated theoretical/empirical predictive method for subcooled flow boiling in annuli with reference to thermal management of ultra-fast electric vehicle charging cables, Int. J. Heat Mass Transfer 175 (2021) 121224, https://doi.org/10.1016/j.ijheatmasstransfer.2021.121224.
[38] W.H. McAdams, W.K. Woods, L.C. Heroman, Vaporization inside horizontal tubes, II. Benzene–oil mixture, Transactions of ASME 64 (1942) 193–200.
[39] W.W. Akers, H.A. Deans, O.K. Crosser, Condensing heat transfer within horizontal tubes, Chem. Eng. Prog. 54 (1958) 89–90.
[40] A. Cicchitti, C. Lombardi, M. Silvestri, G. Soldaini, R. Zavalluilli, Two-phase cooling experiments-pressure drop, heat transfer and burnout measurements, Energia Nucleare 7 (1960) 407–425.
[41] W.L. Owens, Two-phase pressure gradient. Int. Dev. Heat Transfer, Pt. II, ASME, New York, NY, USA, 1961.
[42] A.E. Dukler, M. Wicks, R.G. Cleveland, Frictional pressure drop in two-phase flow: A. A comparison of existing correlations for pressure loss and holdup, AIChE J 10 (1) (1964) 38–43, https://doi.org/10.1002/aic.690100117.
[43] A.E. Dukler, M. Wicks, R.G. Cleveland, Frictional pressure drop in two-phase flow: B. An approach through similarity analysis, AIChE J 10 (1) (1964) 44–51, https://doi.org/10.1002/aic.690100118.
[44] D.R.H. Beattie, P.B. Whalley, A simple two-phase frictional pressure drop calculation method, Int. J. Multiphase Flow 8 (1) (1982) 83–87, https://doi.org/10.1016/0301-9322(82)90009-X.
[45] S. Lin, C.C.K. Kwok, R.Y. Li, Z.H. Chen, Z.Y. Chen, Local frictional pressure drop during vaporization of R-12 through capillary tubes, Int. J. Multiphase Flow 17 (1) (1991) 95–102, https://doi.org/10.1016/0301-9322(91)90072-B.
[46] I. Mudawar, Two-phase flow and heat transfer - lecture notes, Purdue University, West Lafayette, IN, USA, 2015.
[47] S.M. Zivi, Estimation of Steady-State Steam Void-Fraction by Means of the Principle of Minimum Entropy Production, J. Heat Transfer 86 (1964) 247–252.
[48] R.W. Lockhart, R.C. Martinelli, Proposed correlation of data for isothermal two-phase two component flow in pipes, Chem. Eng. Prog. 45 (1949) 39–48.
[49] K. Mishima, T. Hibiki, Some characteristics of air-water two-phase flow in small diameter vertical tubes, Int. J. Multiphase Flow 22 (4) (1996) 703–712, https://doi.org/10.1016/0301-9322(96)00010-9.
[50] H.J. Lee, S.Y. Lee, Pressure drop correlations for two-phase flow within horizontal rectangular channels with small heights, Int. J. Multiphase Flow 27 (5) (2001) 783–796, https://doi.org/10.1016/S0301-9322(00)00050-1.
[51] W. Qu, I. Mudawar, Measurement and prediction of pressure drop in two-phase micro-channel heat sinks, Int. J. Heat Mass Transfer 46 (15) (2003) 2737–2753, https://doi.org/10.1016/S0017-9310(03)00044-9.
[52] J. Lee, I. Mudawar, Two-phase flow in high-heat-flux micro-channel heat sink for refrigeration cooling applications: Part I - Pressure drop characteristics, Int. J. Heat Mass Transfer 48 (5) (2005) 928–940, https://doi.org/10.1016/j.ijheatmasstransfer.2004.09.018.
[53] S.M. Kim, I. Mudawar, Universal approach to predicting two-phase frictional pressure drop for mini/micro-channel saturated flow boiling, Int. J. Heat Mass Transfer 58 (1–2) (2013) 718–734, https://doi.org/10.1016/j.ijheatmasstransfer.2012.11.045.
[54] H. Müller-Steinhagen, K. Heck, A simple friction pressure drop correlation for two-phase flow in pipes, Chemical Engineering and Processing: Process Intensification 20 (6) (1986) 297–308, https://doi.org/10.1016/0255-2701(86)80008-3.
[55] D.S. Jung, R. Radermacher, Prediction of pressure drop during horizontal annular flow boiling of pure and mixed refrigerants, Int. J. Heat Mass Transfer 32 (12) (1989) 2435–2446, https://doi.org/10.1016/0017-9310(89)90203-2.
[56] C.Y. Yang, R.L. Webb, Friction pressure drop of R-12 in small hydraulic diameter extruded aluminum tubes with and without micro-fins, Int. J. Heat Mass Transfer 39 (4) (1996) 801–809, https://doi.org/10.1016/0017-9310(95)00151-4.
[57] C.C. Wang, C.S. Chiang, D.C. Lu, Visual observation of two-phase flow pattern of R-22, R-134a, and R-407C in a 6.5-mm smooth tube, Exp. Therm. Fluid Sci. 15 (4) (1997) 395–405, https://doi.org/10.1016/S0894-1777(97)00007-1.
[58] Y.Y. Yan, T.F. Lin, Evaporation heat transfer and pressure drop of refrigerant R-134a in a small pipe, Int. J. Heat Mass Transfer 41 (24) (1998) 4183–4194, https://doi.org/10.1016/S0017-9310(98)00127-6.
[59] T.N. Tran, M.C. Chyu, M.W. Wambsganss, D.M. France, Two-phase pressure drop of refrigerants during flow boiling in small channels: an experimental investigation and correlation development, Int. J. Multiphase Flow 26 (11) (2000) 1739–1754, https://doi.org/10.1016/S0301-9322(99)00119-6.
[60] W. Yu, D.M. France, M.W. Wambsganss, J.R. Hull, Two-phase pressure drop, boiling heat transfer, and critical heat flux to water in a small-diameter horizontal tube, Int. J. Multiphase Flow 28 (6) (2002) 927–941, https://doi.org/10.1016/S0301-9322(02)00019-8.
[61] L. Sun, K. Mishima, Evaluation analysis of prediction methods for two-phase flow pressure drop in mini-channels, Int. J. Multiphase Flow 35 (1) (2009) 47–54, https://doi.org/10.1016/j.ijmultiphaseflow.2008.08.003.
[62] W. Li, Z. Wu, A general correlation for adiabatic two-phase pressure drop in micro/mini-channels, Int. J. Heat Mass Transfer 53 (13–14) (2010) 2732–2739, https://doi.org/10.1016/j.ijheatmasstransfer.2010.02.029.
[63] W. Li, Z. Wu, Generalized adiabatic pressure drop correlations in evaporative micro/mini-channels, Exp. Therm. Fluid Sci. 35 (6) (2011) 866–872, https://doi.org/10.1016/j.expthermflusci.2010.07.005.

[64] X. Ma, C. Hu, X. Ji, X. Yang, N. Xu, Y. Zhang, J. Wei, Y. Feng, B. Sundén, Flow boiling frictional pressure drop inside micro/mini-channels: A new general model and experimental investigation, Appl. Therm. Eng. 247 (2024) 123111, https://doi.org/10.1016/j.applthermaleng.2024.123111.
[65] W.L. Owens, V.E. Schrock, Local pressure gradients for subcooled boiling of water in vertical tubes, (1960).
[66] N.V. Tarasova, A.I. Leontiev, V.I. Hlopushin, V.M. Orlov, Pressure drop of boiling subcooled water and steam-water mixture flowing in heated channels, in: Proc. Int. Heat Transfer Conf. 3, Begel House Inc., Chicago, USA, 1966, pp. 178–183.
[67] E. Hahne, K. Spindler, H. Skok, A new pressure drop correlation for subcooled flow boiling of refrigerants, Int. J. Heat Mass Transfer 36 (17) (1993) 4267–4274, https://doi.org/10.1016/0017-9310(93)90089-O.
[68] W. Tong, A.E. Bergles, M.K. Jensen, Pressure drop with highly subcooled flow boiling in small-diameter tubes, Exp. Therm. Fluid Sci. 15 (3) (1997) 202–212, https://doi.org/10.1016/S0894-1777(97)00018-6.
[69] P.K. Baburajan, G.S. Bisht, S.K. Gupta, S.V. Prabhu, Measurement of subcooled boiling pressure drop and local heat transfer coefficient in horizontal tube under LPLF conditions, Nucl. Eng. Des. 255 (2013) 169–179, https://doi.org/10.1016/j.nucengdes.2012.10.012.
[70] J. Yan, P. Guo, Q. Bi, Z. Liu, Q. Zhang, Z. Yang, Pressure drop for highly subcooled water flow boiling under high heat and mass fluxes, Appl. Therm. Eng. 124 (2017) 1061–1074, https://doi.org/10.1016/j.applthermaleng.2017.06.096.
[71] B. Ramesh, S. Gedupudi, On the prediction of pressure drop in subcooled flow boiling of water, Appl. Therm. Eng. 155 (2019) 386–396, https://doi.org/10.1016/j.applthermaleng.2019.03.158.
[72] O.I. Abiodun, A. Jantan, A.E. Omolara, K.V. Dada, N.A. Mohamed, H. Arshad, State-of-the-art in artificial neural network applications: A survey, Heliyon 4 (11) (2018) E00938, https://doi.org/10.1016/j.heliyon.2018.e00938.
[73] I.A. Basheer, M. Hajmeer, Artificial neural networks: fundamentals, computing, design, and application, Journal of Microbiological Methods 43 (1) (2000) 3–31, https://doi.org/10.1016/S0167-7012(00)00201-3.
[74] S. Guanghui, K. Morita, K. Fukuda, M. Pidduck, J. Dounan, J. Miettinen, Analysis of the critical heat flux in round vertical tubes under low pressure and flow oscillation conditions. Applications of artificial neural network, Nucl. Eng. Des. 220 (1) (2003) 17–35, https://doi.org/10.1016/S0029-5493(02)00304-7.
[75] Y. Qiu, D. Garg, L. Zhou, C.R. Kharangate, S.M. Kim, I. Mudawar, An artificial neural network model to predict mini/micro-channels saturated flow boiling heat transfer coefficient based on universal consolidated data, Int. J. Heat Mass Transfer 149 (2020), https://doi.org/10.1016/j.ijheatmasstransfer.2019.119211.
[76] Y. Qiu, T. Vo, D. Garg, H. Lee, C.R. Kharangate, A systematic approach to optimization of ANN model parameters to predict flow boiling heat transfer coefficient in mini/micro-channel heatsinks, Int. J. Heat Mass Transfer 202 (2023) 123728, https://doi.org/10.1016/j.ijheatmasstransfer.2022.123728.
[77] E. Cho, H. Lee, M. Kang, D. Jung, G. Lee, S. Lee, C.R. Kharangate, H. Ha, S. Huh, H. Lee, A neural network model for free-falling condensation heat transfer in the presence of non-condensable gases, Int. J. Therm. Sci. 171 (2022) 107202, https://doi.org/10.1016/j.ijthermalsci.2021.107202.
[78] W.S. McCulloch, W. Pitts, A logical calculus of the ideas immanent in nervous activity, The Bulletin of Mathematical Biophysics 5 (4) (1943) 115–133, https://doi.org/10.1007/BF02478259.
[79] A.D. Rasamoelina, F. Adjailia, P. Sincak, A review of activation function for artificial neural network, in: 2020 IEEE 18th World Symposium on Applied Machine Intelligence and Informatics (SAMI), IEEE, Herlany, Slovakia, 2020, pp. 281–286, https://doi.org/10.1109/SAMI48414.2020.9108717.
[80] D.E. Rumelhart, G.E. Hinton, R.J. Williams, Learning representations by back-propagating errors, Nature 323 (6088) (1986) 533–536, https://doi.org/10.1038/323533a0.
[81] D.P. Kingma, J. Ba, Adam: A method for stochastic optimization, (2014).
[82] H.J. Seltman, Experimental Design and Analysis, Department of Statistics, Carnegie Mellon University, 2018.
[83] The MathWorks Inc., Deep Learning Toolbox version: 14.5 (R2022b), (2022).